QATAR UNIVERSITY

COLLEGE OF ARTS AND SCIENCES

PREPARATION OF POLYSTYRENE/ NICKEL OXIDE NANOCOMPOSITE SUPERHYDROPHOBIC COATING FOR PROTECTION AGAINST CORROSION

BY

CHERIVA AHMED MANNAH

A Thesis Submitted to

the Collage of the College of Arts and Sciences

in Partial Fulfillment of the Requirements for the Degree of

Masters of Science in Material Science and Technology

January 2020

COMMITTEE PAGE

The members of the Committee approve the Thesis of
Cheriva Mannah defended on 20/11/2019.

Dr. Aboubakr Abdullah
Thesis/Dissertation Supervisor

Dr. Talal Altahtamouni
Committee Member

Dr. Mohammad K. Hassan
Committee Member

Dr. Abdul Shakoor
Committee Member

Approved:

Prof. Ibrahim AlKaabi, Dean, College of College of Arts and Sciences

ABSTRACT

MANNAH, CHERIVA, AHMED., Masters : January 2020, Material Science and Technology

Title: PREPARATION OF POLYSTYRENE/ NICKEL OXIDE NANOCOMPOSITE SUPERHYDROPHOBIC COATING FOR PROTECTION AGAINST CORROSION

Supervisor of Thesis: Dr. Aboubakr. M. Abdullah

Many technologies have been studied carefully to overcome the corrosion phenomenon of various metal species found in nature. Among these, the high water repellent surfaces have received significant attention from researchers and industrialists from the last few decades. These surfaces are known as superhydrophobic surfaces that have high WCA >150° and low CAH<10°. Herein, Polystyrene/Nickel oxide (PS-NiO) nanocomposite superhydrophobic coatings are produced using a one-step electrospinning technique. Three coatings were fabricated to study the effect of varying NiO nanoparticles concentrations on the wettability of polystyrene coating. The morphology, hydrophobicity behavior, structures, and thermal properties of PS/NiO nanocomposite coatings were investigated. It was found that the presence of NiO nanoparticles enhances various features of polystyrene coating. A high water contact angle of 155° ± 2° and low contact angle hysteresis of 5° was achieved. Also, corrosion resistance performance of PS/NiO nanocomposite coating was evaluated using the EIS technique. The observations showed that the addition of NiO nanoparticle highly enhances the corrosion protection efficiency of PS coating.

DEDICATION

With all my love, I dedicate the success of this work to my ideal father, Ahmed, my husband, and my family members who have shown absolute affection, love, encouragement, and prays that made me able to achieve my objectives and goals.

ACKNOWLEDGMENTS

I want to express my sincere and most profound appreciation to my supervisor Dr. Aboubakr Abdullah for his guidance and support over this work. His suggestions and thoughts were precious toward the success of this work. I am extremely thankful to my committee members Dr. Talal Altahtamouni, Dr. Mohammad Hassan, and Dr. Abdul Shakoor, for their advice and assistance. A great thanks go to Mr. Ahmed Bahgat for his patience; he showed constant support and the perfect guide to me during the lab work.

I would like to extend my sincere appreciation to the faculty members of Material Science and Technology program at Qatar University: Dr. Ahmed Elzatahry, Dr. Khalid Youssef and Dr. Igor Kurba for their effort during my master's study journey as well as the staff of Center for Advanced Materials, CAM, and Central Laboratory Unit, CLU, for their cooperation through the period of work.

I want to convey my gratitude and thanks to my family, my husband, and friends for their support, understanding, patience, and help during these years, without which this work would not have been completed.

TABLE OF CONTENTS

DEDICATION iv

ACKNOWLEDGMENTS v

LIST OF TABLES ix

LIST OF FIGURES x

Chapter 1: Introduction 1

Chapter 2: Literature review 5

2.1 Superhydrophobic surfaces 5

2.2 Models of superhydrophobic states 5

2.2.1 Surface models of wetting on rough surfaces 6

2.2.2 Surface energy 7

2.2.3 Contact angle hysteresis 7

2.3 Techniques for fabricating superhydrophobic coatings 9

2.3.1 Sol-gel processing methods 10

2.3.2 Etching 10

2.3.3 Electrochemical reaction and deposition 11

2.3.4 Electrospinning 13

2.3.4.1. Parameters effecting electrospinning 14

2.4 Applications of superhydrophobic surfaces 18

2.4.1 Increase of corrosion resistance 18

2.4.2 Oil and water separation 19

2.4.3 Self-cleaning surfaces 20

2.4.4 Anti-bacterial surfaces 21

2.4.5 Other applications 22

chapter 3: Experimental 25

3.1 Material 25

3.2. Sample preparation 25

3.2.1 Synthesis of PS-NiO superhydrophobic coating 25

3.2.2 Electrospinning technique 26

..... 27

3.3 Characterization Methods 27

3.3.1 Scanning Electron Microscopy (SEM) and EDX 27

3.3.2 Atomic Force Microscopy (AFM) 28

3.3.3 Fourier Transform Infrared Spectroscopy (FTIR) 29

3.3.4 X-Ray Diffraction (XRD) 30

3.3.5 Contact Angle Measurement 31

3.3.6 Differential Scanning Calorimetry (DSC) 32

3.3.7 Thermogravimetric Analysis (TGA) 33

3.3.8 Electrochemical impedance spectroscopy (EIS) 34

..... 35

chapter 4: Result and Discussion 36

4.1. Structure and Morphology 36

4.1.1. Scanning Electron Microscopy (SEM) 36

4.1.2 Contact Angle Measurement 40

4.1.3. Atomic Force Microscopy (AFM) 43

4.1.4. Fourier Transformation Infrared Spectroscopy (FTIR) 44

4.1.5. X-Ray Diffraction 46

4.2. Thermal Properties 47

4.2.1 Differential scanning calorimetry (DSC) 47

4.2.2. Thermogravimetric analysis (TGA) 49

4.3 Electrochemical Impedance Spectroscopy (EIS) 51

Chapter 5: Conclusion 56

References 59

LIST OF TABLES

Table 2.1. Summary of the most common electrospun polymers producing nanofiber structures……..…17

Table 2.2 Examples of recent publications of superhydrophobic surface and their applications…….23

Table 3.1. compositions and electrospinning parameters for pure Polystyrene (PS) and PS/NiO nanocomposite superhydrophobic coatings (SHC).……..26

Table 4.1. The average diameter of the nanofibers of Pure PS and PS/NiO nanocomposite coatings……. 38

Table 4.2. Water contact angle (WCA) and water contact angle hysteresis (WCAH) of the prepared PS and PS/NiO SHCs…….…..…….43

Table 4.3. DSC data for pure PS and PS/NiO nanocomposite SHCs…….48

Table 4.4. TGA data of PS and PS/NiO nanocomposite SHCs…….49

Table 4.5. Electrochemical parameters from Nyquist and Bode plots for aluminum substrates coated with pure PS and PS/NiO SHCs……53

LIST OF FIGURES

Figure 2.1. Wetting states of a liquid droplet (a) Young's (b) Wenzel and (c) Cassie-Baxter……..…6

Figure 2.2. A schematic description of some of the parameters that affecting the force needed for a droplet to start sliding on a tilted surface……...8

Figure 2.3. A superhydrophobic surface prepared by chemical etching process……..11

Figure 2.4. (A) Effect of electrodeposition time, (B) effect of electrodeposition potential on WCA and CAH…….12

Figure 2.5. Electrospinning setup…….14

Figure 3.1. Electrospinning equipment…….26

Figure 3.2. Coated samples prepared via electrospinning technique……...27

Figure 3.3. Scanning Electron Microscopy……..28

Figure 3.4. Atomic Force Microscopy……. ..….29

Figure 3.5. FTIR instrument model: PerkinElmer Frontier……30

Figure 3.6. The PAN analytical X-Ray diffractometer……...……..31

Figure 3.7. Optical Contact angle…….……..32

Figure 3.8. Differential Scanning Calorimeter …….……..33

Figure 3.9. Thermogravimetric analysis device……..…...….34

Figure 3.10. Gamry Potentiostat Reference 3000……..……...…….……35

Figure 4.1. SEM images of electrospun PS and PS/NiO nanocomposite superhydrophobic coatings…….37

Figure.4.2. SEM-EDX mapping micrographs and spectra of PS and PS/Nio nanocomposite SHCs……..39

Figure 4.3. water contact angle measurements for pure PS and PS/NiO nanocomposite SHCs……...42

Figure 4.4.. AFM images of the surface of (a) PS, (b) PSNI-1, (c) PSNI-2 and (d) PSNI-3……..44

Figure 4.5. FTIR spectra for pure PS and polystyrene/NiO nanocomposite superhydrophobic coatings…….45

Figure 4.6. X-ray diffraction pattern of polystyrene/NiO nanocomposite superhydrophobic coating……...46

Figure 4.7. DSC analysis for polystyrene and polystyrene/NiO nanocomposites (a) Heating curve (b) Cooling curve…….48

Figure 4.8. Thermogravimetric Analysis for pure PS and PS/NiO nanocomposite Super-hydrophobic coatings……..50

Figure 4.9. Equivalent electrical circuit used to fit the EIS spectra of Polystyrene and PS/NiO SHC in 3.5 wt % NaCl……....54

Figure4.10. Nyquist Plots of EIS measurements of (a) PS, (b) PSNI-1, (c) PSNI-2 and (d) PSNI-3 in 3.5 wt% NaCl……..54

Figure 4.11. Bode plots of EIS measurements of (a) PS, (b) PSNI-1 (c) PSNI-2 and (d) PSNI-3 in 3.5 wt% NaCl……..55

CHAPTER 1: INTRODUCTION

Corrosion is a natural phenomenon that occurs due to an irreversible reaction of metal with its surrounding environment in the presence of humidity and oxygen. Many industries are suffering from corrosion problems, which cause a high maintenance coast, less plant efficiency, and severe safety issues [1]. Also, the low efficiency resulted from corroded components affects the performance of the plants rapidly because of the chemical and mechanical properties changes. Hence, surface properties modification sometimes is required in such conditions. This could be achieved either by applying several types of coatings and/or inhibitors. The coatings are economically a superior choice with a low impact on the running cost compared with the modification of the bulk properties [2].

Aluminum (Al) and its alloys (AAs) have substantial usage in many industrial areas ranging from the thin aluminum foil in the packaging industry to the highly strong materials for aircraft and automotive [3]. The diversity of aluminum alloy applications arises from the different alloying elements added to pure aluminum such as copper, silicon, magnesium, manganese, nickel, and zinc. This alloying process results in unique characteristics such as high mechanical strength, good thermal and electrical conductor as well as quite corrosion resistance against uniform corrosion because of the presence oxide layer on the surface of aluminum metal substrates[4][5]. However, aluminum alloys are significantly prone to localized corrosion. Consequently, corrosion protection inhibitors are involved in protecting aluminum from corrosion, especially in the oil and gas industries [6].

For example, many inhibitors are used to protect the metal surface from corrosive environments. Inhibitors are adsorbed form a uniform film similar to a coating that acts as a physical barrier. Usually, the inhibitors lose their efficiency with time due to

desorption. So, different protective coatings, depending on the different types of applications, can be used to prevent the metal components from corrosion [7]. Organic coatings are one category, which can be classified according to the resin binder that controls protectiveness and resistance to degradation. They display a perfect corrosion prevention performance even if the metal is placed in a corrosive environment [8]. Adhesion between the organic coatings and metal substrates played a significant factor as an anti-corrosion material, particularly in the humid surroundings where the sample may be exposed to some water drops which may react with the coating and impact its resistance. [9].

Recently, superhydrophobic surfaces received great attention in different fields from surface physics, surface chemistry, and materials science, and engineering. A surface with high water repellent generated by applying a micro-patterned roughness combined with low surface energy material known as a superhydrophobic surface. The superhydrophobic property of the coating depends on two main surface properties: surface energy and surface roughness[10][11]. In addition, the essential factor that characterizes the hydrophobic phenomenon is the static contact angle. This angle is the angle that a liquid droplet makes with a solid surface. The superhydrophobic surface has a water contact angle (WCA) >150˚ and low contact angle hysteresis (WCAH) < 10^{o}. The WCA can be controlled by number of factors: such as surface roughness, sample polishing, and surface cleanliness [12]. Superhydrophobic coatings have higher efficiency compared to inhibitors because they reduce the water contact angle with the surface which results in decreasing the oxidation reaction frequency that can take place as result of repelling the electrolyte and decrease the electrolyte permeation within the coating or at least by reducing the residence time of the electrolyte within which the electrolyte is in contact with the metal surface.

Several pieces of research have reported the effectiveness of generating superhydrophobic coating using polymers. Polystyrene and poly-functionalized polystyrene are widely used in different applications such as packaging, electronic applications, toys, households, goods, etc. [13]. PS is relatively cheap and has a low melting point, which results in the broader use of PS in different applications [13]. Their chemistry has been improved by chemical modification using acetic anhydride and epichlorohydrin with the existence of catalysts. This results in better adhesion and anticorrosion properties[14]. compositing polystyrene with coated nanoparticles such as silica obtained around a 20% decrease in specific surface area compared to pure polystyrene [15]. PS/nanoparticle nanocomposite enhances the surface morphology and hydrophobicity of materials. For example, Simsic et al. revealed the effect of the surface roughness on the degree of super hydrophobicity of materials by fabricating polymeric nonwoven fibers with high surface roughness through the electrospinning process [16]. Also there are many studies revealed that the fabrication process of superhydrophobic coatings by adding inorganic nanoparticles to PS, including PS/SiO_2 [17], PS/TiO [18], PS/MnO_2 [19] and PS/Al_2O_3 [20]. In fact, the addition of these nanomaterials shows a significant improvement of the surface roughness with decreasing the surface energy of the produced coating as well as facilitating the formation of the hierarchical shapes [21]. In this project, new NiO nanoparticles/polystyrene nanocomposite superhydrophobic coating was prepared using electrospinning for the first time targeting improving the corrosion protection efficiency of polystyrene coatings. This work provides a full materials and electrochemical characterization study for the effect of compositing polystyrene with NiO nanoparticles, which reveals the high corrosion resistance of this new coating.

Electrospinning techniques are commonly used to produce superhydrophobic

coasts due to its simplicity, high efficiency, template synthesis, self-assembly, inexpensive, and applicable for plenty of polymers to generate nanofibers [22], [23] [24], [25]. Besides the chemical nature of the SHCs, many physical properties directly affect the performance of a SHC. For example, the solution viscosity, surface tension and average molecular weight of used polymer, and operational electrospinning parameters such as solution flow rate, applied voltage, distance between a needle and substrates and time are main key parameters [26],[27], [28], [29], [30].

The purpose of this work is to fabricate a superhydrophobic coating of PS/NiO nanocomposite for protection against corrosion for aluminum substrates via electrospinning technique. This thesis shows the preparation methods of PS/NiO nanocomposite superhydrophobic coating and all the required characterization techniques which were used to study the properties of the coatings including the structure of the samples using the XRD, The surface roughness, morphology and the composition of the coatings using AFM, SEM, and EDX respectively. Also, the thermal properties of the samples were tested by DSC and TGA. Water contact angle (WCA) and contact angle hysteresis (CAH) were employed to evaluate the surface liquid tension and the degree of hydrophobicity. Finally, the electrochemical impedance spectroscopy (EIS) technique was applied to examine corrosion resistance of the prepared SHC nanocomposite coatings.

CHAPTER 2: LITERATURE REVIEW

2.1 Superhydrophobic surfaces

Superhydrophobic surfaces are highly water repellent ones that have a water contact angle higher than 150° and very low contact angle hysteresis less than 10°. There are many examples of superhydrophobic materials in natures, such as lotus leaves, insect wings, and animal fur [31][32][33]. These micro- or nanostructure surfaces are covered with low surface energy materials that can make an interfacial line with liquid by keep holding air on the rough surface, which results in a reduction in the water contact angle [34]. Therefore, those non-wetted surfaces become fertile materials in different corrosion applications since the trapped air in the superhydrophobic surfaces can protect the aggressive ions from being in contact with the metal surface [35]. Generally, the superhydrophobic surface usually consists of a combination of hydrophobic material and micro or nanoparticles [36][37].

2.2 Models of superhydrophobic states

To clarify the parameters that modeled superhydrophobic coatings, it is necessary to explain the basic principle behind this phenomenon. When a liquid droplet interacts with a metal surface, it can be described by contact angle measurement [38]. The intersect of the water droplet, and the coating surface contact angle is calculated by Young's equation[39] [40]:

$$\cos\theta_Y = \frac{\gamma_{SV}-\gamma_{SL}}{\gamma_{LV}} \qquad (2.1)$$

Where, θ_Y is the contact angle in Young's mode, $\gamma_{SV}, \gamma_{SL}\ and\ \gamma_{LV}$ represent the surface energies corresponded to solid-vapor, solid-liquid, and liquid-vapor interfaces, respectively. If the surface shows water contact angle $\theta < 90°$ is hydrophilic while if the surface exhibit water contact angle $\theta > 90°$ is hydrophobic and if the surface shows water contact angle $\theta > 150°$ known as superhydrophobic surface.

2.2.1 Surface models of wetting on rough surfaces

One of the most critical parameters that modeled the SHSs is surface roughness. How the rough hydrophobic surface interacts with a liquid droplet can be described by either Wenzel or Cassie-Baxter state [23]. The Wenzel state takes place when a liquid droplet is thoroughly permeated through the rough surface, which will increase the solid-liquid interfacial area [41]. Also, the Wenzel state can be considered as homogenous wetting because the resulting interface surface consists of only liquid-solid contact [42]. On the other hand, Cassie-Baxter state takes place when a liquid droplet rests on the top of the rough surface trapping air in the hierarchical structure of the coating, forming a heterogeneous interfacial consist of solid-liquid and liquid-gas below the droplet. The two wetting states are shown in Figure 2.1.

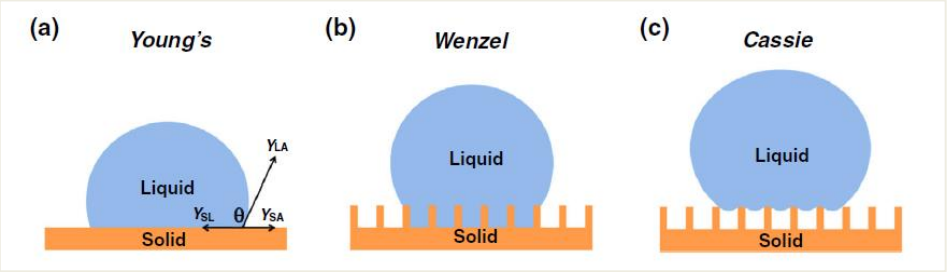

Figure 2.1. Wetting states of liquid droplet (a) Young's (b) Wenzel and (c) Cassie-Baxte

Consequently, the superhydrophobic surfaces must show water contact angle >150° and water contact angle hysteresis <10° [43]. The interface of the metal that interacts with liquid droplets in the Wenzel state cannot be considered as superhydrophobic even it may show a high water contact angle but will never exhibit

low contact angle hysteresis because of the contact line pinning. While Cassie-Baxter states allow liquid droplets to freely move on the surface, which can be considered as a superhydrophobic state [44][45]. Taylor et al. reported the highest water contact angle of the smooth surface is around 115°; as a result, to increase the water contact angle to reach superhydrophobic state, more roughness is needed [38].

2.2.2 Surface energy

Low surface energy is a substantial mark that characterizes the superhydrophobic behavior of the materials. Several types of surfactants were widely used for reducing the surface energy of the materials in various applications. For instant. Alkanethiols have been used as an active surfactant for decreasing surface energy, which provides a hydrophobic alkyl chain as well as a thiol group on the surface of the materials [46]. Furthermore, silane groups were commonly employed for the reduction of surface energy. Particularly, fluoroalkyl silanes received high consideration due to the existence of CF2 and CF3 groups, which are very effective in the lowering of materials surface energy [47]. Also, organic silane was used in surface treatment by providing hydroxyl groups. However, fluoroalkyl silanes are very expensive and causing hazards to the environment because of the existence of fluorine. Other substances were recommended to be used for surface modification, such as stearic acid and polymers [48].

2.2.3 Contact angle hysteresis

The formation of three heterogeneous states and highly roughness surfaces reflect the degree of the superhydrophobicity of the material with very low contact angle hysteresis. Cassie-Baxter state represents SHSs due to the impact of the contact angle and the allowance of the contact line to pin on the surface resulting in several values of the contact angle [49]. The calculated difference between the maximum and minimum

values of this range predict contact angle hysteresis (CAH). Contact angle hysteresis can be calculated by two methods, including the variation of the sessile-drop approach and the tilting plate procedure [39]. In the variation of the sessile-drop method, the advancing contact angle can be predicted by increasing the volume of a liquid droplet slightly while receding angle (RA) can be found by reducing the volume of the water droplet causing recede. The difference between the highest advancing and the lowest receding contact angels called contact angle hysteresis (CAH) [50]. Furthermore, in the tilting plate method, the surface is set at a specific sliding angle to roll the droplet directly when it touches the surface. The contact angle of the droplet in the moving direction is referred to advancing angle (θ_{Adv}) and the contact angle in the opposite direction is indicated receding contact angle (θ_{Rec}) [51]. Hence, an increasing in the difference between θ_{Adv} and θ_{Rec} will rise the tilting angle which means the adhesion between the surface and the liquid increase and larger CAH is achieved. The force required for a liquid droplet to start sliding on a surface is illustrated by Figure 2. 2 and Equation 2.

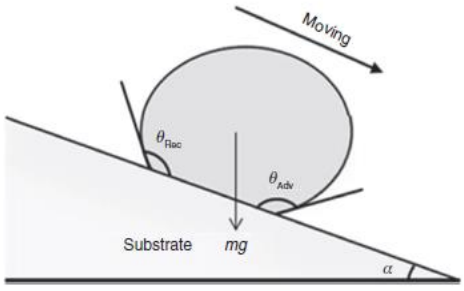

Figure 2.2. A schematic description of some of the parameters that affecting the force needed for a droplet to start sliding on a tilted surface

$$F = \frac{mg \sin\alpha}{d} = \gamma_{lv}(\cos\theta_R - \cos\theta_A) \qquad (2.2)$$

Where α is the sliding angle, γ_{lv} is the surface tension of the liquid, $\theta_R \; and \; \theta_A$ are the receding and advancing CA, respectively. d is the width of the droplet perpendicular to the moving direction, m is the mass of the droplet, and g is the gravitational acceleration [52].

As noted above, superhydrophobic surfaces must have an extremely small sliding angle. In another word, at very low CAH, approximately zero, the water droplet will quickly roll off as soon as the substrate is placed on an inclined plane. However, many superhydrophobic surfaces showed some hysteresis resulting from friction caused by the heterogeneity of the surface, but CAH can be controlled by roughening the surface on the micro and nanoscales [53].

2.3 Techniques for fabricating superhydrophobic coatings

Nowadays, superhydrophobic coatings receive a valuable tension that made them widely prepared by different techniques using various materials, including organic materials and inorganic materials. Sometimes surface treatment such as roughening a surface of the material is required even though the materials are inherently hydrophobic like organic materials. Several techniques have been used for the fabrication of superhydrophobic coatings which can be divided into two categories [54]:

(a) Enhancing the surface roughness of the materials which have a low surface energy

(b) Chemically adjusting a rough surface with low surface energy materials.

To date, numerous techniques have been investigated for the fabrication of superhydrophobic surfaces with high roughness and low surface energy such as sol-gel

process [55], chemical etching[56], electrochemical decomposition [57], plasma polymerization [52], layer-by-layer assembly [58], chemical vapor deposition [59] and electrospinning [60].

2.3.1 Sol-gel processing methods

The sol-gel method was used in several applications to fabricate superhydrophobic coatings in a wide range [61]. The preparation process is explained by some examples of the structuration of an oxide network by the polycondensation reaction of molecular precursors in a liquid. The liquid molecules are blended with colloidal particles via Vander Waals forces or hydrogen bonds [62]. Wang et al. synthesized a superhydrophobic membrane using a variable concentration of tetraethyl orthosilicate (TEOS) and trimethylethoxysilane (TMES) with the addition of ammonia hydroxide (NH_4OH) and ethanol. The resulted silica sol was used to pretreat a steel sheet by spray deposition then dried in an oven for 1 hr [63]. They found out this superhydrophobic coating display an excellent corrosion resistance in 3.5 wt% NaCl aqueous solution. However, only one formed composition showed WCA around 158 but with low corrosion resistance. In fact, chemical composition and surface morphology of SHS played a significant effect on corrosion prevention [64]. For this reason, a surface with a high water contact angle not essentially means high corrosion resistance. Sol-gel technique is simple and low-cost, but the method is slow, which may need a long time to be finished [65].

2.3.2 Etching

The etching process is a popular and effective way to prepare heterogeneous and high rough surfaces, as shown in Figure 2.3. There are several etching methods, including acid and base [66], chemical, electrochemical, ionic, and plasma etching [67]. Recently, laser, chemical and plasma etching have been used to construct

superhydrophobic surfaces [68]. For instance, Teshima et al. fabricated a transparent superhydrophobic surface from a polyethylene terephthalate (PET) through selective oxygen plasma etching and plasma-enhanced vapor deposition using a particular precursor such as tetramethylsilane [69]. Moreover, Qian and Shen reported an easy process for preparing high roughening surfaces by treating aluminum substrates through dislocation chemical etching. Then the samples were treated with fluoroalkyl silane and exhibit superhydrophobic behavior [70].

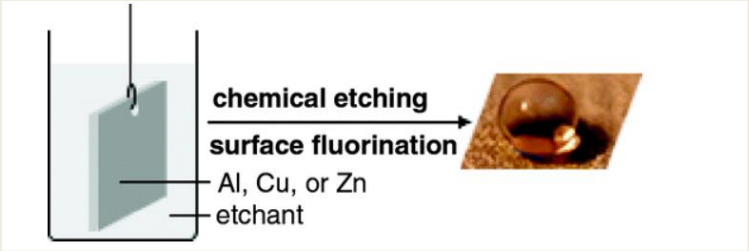

Figure 2.3. A superhydrophobic surface prepared by chemical etching process.

2.3.3 Electrochemical reaction and deposition

Superhydrophobic coatings can be generated by electrochemical reactions and depositions. This method is widely used to prepare micro/nanostructures because it is cheap, fast, and easy in operations at low temperatures [71]. The electrodeposition preparation of anti-corrosion surfaces can be designed either by applying particular external potential between two electrodes or by using galvanic ionic exchange between substrate and ions [72]. Liu et al. fabricated a superhydrophobic coating by depositing of 1-dodecanethiol/polydopamine multi-layer films on copper substrates. The resulted superhydrophobic surfaces showed WCA around 154° with high corrosion resistance

efficiency of 99% in 3.5 wt% NaCl solution [73]. The main parameters to control the electrodeposition are the distance between the anodic ion and cathodic substrate, the electrodeposition time, and the electrodeposition applied voltage. Zhang et al. noticed that by keeping the distance between the anodic platinum plate and cathodic aluminum substrates at 2 cm increase WCA up to 162.1[74]. Also, they mentioned that by keeping the electrodeposition time between 5 and 180 min, the water contact angle remains higher than 150° and the sliding angle lower than 3°. While if the deposition time increased to 210 min or higher, the WCA was reduced to 139.9 and lower as described by Figure 1 a [74]. This is due to the change in the surface morphology with time from heterogeneous to homogenous due to the agglomeration of large particle size of monomer papillae. Besides, the water contact angle decreases as the electrodeposition applied voltage increases at a constant time [75]. It was found that the optimum voltage which leads to a perfect superhydrophobic coating was around 20 V as a result of the production of the hierarchical micro/nanoholes on the surface of Al. Although, when the applied voltage was raised to 50 V or more the water contact angle was decreased to 103.5 as shown in figure 2.4 (B).

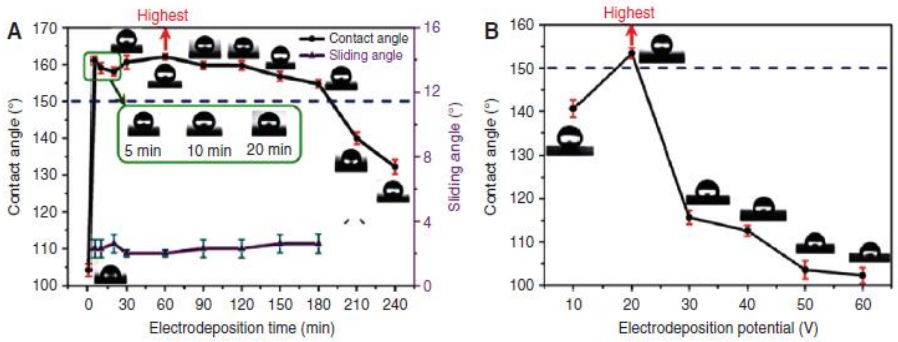

Figure 2.4. (A) Effect of electrodeposition time, (B) applied effect electrodeposition potential on WCA and CAH.

2.3.4 Electrospinning

Electrospinning is a simple, effective, and low-cost method that becomes widely employed to produce continuous polymer nano/microfibers on large scales of natural polymers and synthetic polymers. The term ″electrospinning″ was extracted from the ″electrostatic spinning″ that recently used, while the fundamental idea was published by Formalas in 1934-1944 when he established an experimental system for the fabrication of polymer filaments by applying an electrostatic force [26]. In recent years, the electrospinning technique received significant attention due to the high interest in nanotechnology, as it is easily used to yield fibers structures of several polymers with small average diameters around submicron or nanometers. Polymeric nanofibers with 10 to 100 nm of diameter show unusual characteristics such as the large surface area to volume ratio, facile surface modification, and excellent mechanical performance [26][76]. In the electrospinning process, an electric potential is used to stretch the polymeric solution droplet from the end of the spinneret (needle) to the collector plate. At the point when the applied electric field get rids of the surface tension of the solution droplet, the charged jet of the polymer solution is ejected and gain bending stabilities resulted from the repulsive force between the charged carrier and the jet. Then the jet raises longer and thinner to be collected by the collector plate as nanofibers [77]. There are two well-known configurations for electrospinning classified based on the way that syringe is fixed to spin polymer solution: horizontal or vertical arrangement. The horizontal electrospinning configuration is shown in Figure 2.5. Acatay et al. prepared an electrospun film made up of a continuous web of different aligned fibers via electrospinning method. They applied an electric field from the tip of the needle to the collector plate to spin the thermoset fluorinated polymer on the aluminum substrates [78].

Nanofibers morphology, electrical and mechanical properties can be affected by polymeric solution properties and operating parameters of electrospinning such as polymer molecular weight and concentration, applied electric field, solution flow rate, the distance between the tip of the needle and the collector and the inner diameter of the needle [79]. Moreover, this technique becomes widely used in several fields such as filtration, drug delivery, enzyme carriers, biosensors, affinity membrane, and recovery of metal ions, energy storage, wound healing, and different engineering sectors [80].

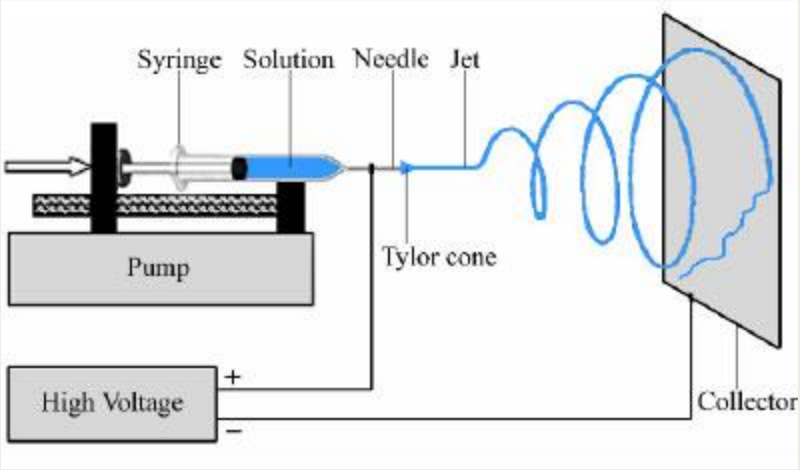

Figure 2.5. Horizontal electrospinning setup

2.3.4.1. Parameters affecting electrospinning

2.3.4.1.1 Concentration of polymeric solution

The polymeric solution concentration is an essential parameter that determines if the prepared solution can be electrospun into nanofibers. Also, it profoundly affects the morphology of the electrospun fibers. There is an optimum concentration for each solution depending on the molecular weight of the polymer and solvent used. Reaching this concentration provides a nanofiber structure without beads [81]. As the

electrospinning technique involves electrical charges transfer from the electrode to the spinneret, minimal electrical conductivity is needed for nanofiber construction. The electrical conductivity of the polymer solution is directly affected by the concentration of the electrospun polymer [82]. Also, the rheological properties of the polymeric solution, particularly viscosity, impact the formation of nanofibers. Hence, the solution with high viscosity cannot be pumped by the syringe whereas the solutions with very low viscosity are not able to generate fibers. The viscoelastic force applied by the polymer charged jet is the main fore that act against the columbic repulsion force, which is the critical force that elongates the jet. Also, low polymeric solution concentration caused fiber defects such as beaded fibers due to the effect of surface tension. Several types of research have studied the impact of polymeric solution concentration on the size of electrospun fibers, and it was found that the fiber diameters increase with increasing polymer concentration [27][83].

2.3.4.1.2 Applied voltage effect

The applied voltage has a remarkable effect on the fiber morphology since it affects the polymer mass ejected out of the spinneret tip. The higher the applied voltage, the larger the fiber diameters will be as more polymer will be ejected. Besides, beads formation and generation of a second jet become easier to take place. For instance, Chen et al. reported that the fiber diameters increase about $8\mu m$ when the electrospun applied voltage increases from 10 kV to 16 kV [84]. However, increasing the applied voltage can present more charges on the solution surface and become more stretched by the jet, which causes a reduction in the nanofiber diameters as well as increases the electrostatic repulsive force on the fluid jet [80].

2.3.4.1.3 Volume Feed-Rate effect

The rate of the feed solution is considered the most serious element that affects the

jet velocity and the morphology of the produced fibers. At low flow rate the fibers fabricated show large diameters and a decreased uniformity. On the other hand, a high feeding rate leads to the formation of beads and causes fiber defects such as small fibers with large diameters. Moreover, for volatile solvents and fabrication of solid nanofibers low flow rate is preferable. In general, feeding rate should be in harmony with the removing rate of the solution from tip, where small flow rates can inhibit the electrospinning process while high flow rates lead to the formation of beaded fiber structure as a result of the decrease of time available for the solvent evaporating before reaching the collector [80].

2.3.4.1.4 Tip-to-collector Distance effect

The distance between the needle tip and the ground collector has a considerable effect on the fiber morphology. Increasing the working distance to an optimum one results in small diameter and uniform fiber structure. On the other hand, decreasing this distance causes a high electric field, which produces fibers with different diameters and reduces uniformity. Furthermore, more beads are formed when the working distance is decreased which provides a beaded fiber structure [84].

2.3.5. Surface Chemistry Control

In general, many substrates with rough surfaces do not exhibit superhydrophobic behavior due to high surface energy of the prepared coating, so they must be treated with low surface energy materials to decrease surface energy of the coating including fluorocarbons, silicones and some organic materials such as polyethylene, polypropylene, and polystyrene, etc. However, some inorganic materials such as ZnO, TiO, and Al_2O_3 nanoparticles, which have high surface energy, can be smoothly covered by airborne organic contaminants. Therefore these nanoparticles can be used to modify the surfaces and show superhydrophobicity [20][85][86]. The most famous

electrospun polymers are summarized in Table 2.1.

Table 2.1. The summary of most common electrospun polymers producing nanofiber structures

Polymer	Solvent	Concentration	Ref
Polyethylene Terphtalete (PET)	Dichloromethane and trifluoroacetic acid (1:1)	12-18 wt%	[87]
Polyacrylic acid-polypyrene methanol (PAA-PM)	Dimethylformamide	-	[87]
Polystyrene (PS)	Tetrahydrofuran, Dimethylformamide, Toluene	18-35 wt%	[88][89]
Polyamide (PA)	Dimethylacetamide	-	[90]
Polymethacrylate(PMMA)	Tetrahydrofuran, acetone, chloroform	-	[88]
Polyvinyl phenol (PVP)	Tetrahydrofuran	20-60 %(wt/vol)	[91]
Polyvinylchloride (PVC)	Tetrahydrofuran, Dimethylformamide	10-15 wt%	[92]
Poly-vinylidene-fluoride (PVDF)	Dimethylformamide, Dimethylacetamide	20 wt%	[93]
Polyetherimide (PEI)	Hexafluoro-2-propanol	10 wt%	[94]
Polyethylene glycol (PEG)	Chloroform	0.5-30 wt%	[95]
Poly (ethylene-co-vinyl alcohol)	Isopropanol/water (70/30) %v/v	2.5-20 %w/v	[96]
Polyethylene Oxide (PEO)	Distilled water	7-10 %wt	[97]
Polyvinyl alcohol (PVA)	Distilled water	8-16 %wt	[98][94]
Polyacrylonitrile (PAN)	Dimethylformamide	600 mg	[99][100]
Polycarbonate (PC)	Dimethylformamide,	10 %wt	[101]

Polymer	Solvent	Concentration	Ref
Polybenzimidazole, (PBI)	Dimethylacetamide	10 %wt	
Poly(hydroxybutyrate-co-hydroxyvalerate) (PHBV)	chloroform	15-20 %wt	[102]
Polyurethane (PU)	Dimethylformamide	10 %wt	[103][104]
Nylon 6,6,PA-6,6	Formic acid	10 %wt	[105]

2.4 Applications of superhydrophobic surfaces

A detailed review of literature about superhydrophobic materials has been carried out and is presented here.

Superhydrophobic materials with excellent water repellency have attracted much interest in many areas of self-cleaning, oil-water separation, corrosion resistance, and Antibacterial applications [106][107][108].

2.4.1 Increase of corrosion resistance

Corrosion is a well know phenomenon that causes metallic materials degradation. Anti-corrosion coatings were well investigated by applying several methods to control the corrosion rate on the metal surfaces. Recently, superhydrophobic surfaces were studied to inhibit corrosion on a wide range of materials such as steel, aluminum, copper and magnesium. [109].

Li et al. [110] fabricated stable Ni-Al_4Ni_3-Al_2O_3 superhydrophobic surface on aluminum substrates using etching technique, followed by replacement deposition and then annealing. They investigated the anti-corrosion behaviors of the samples via Tafel extrapolation and electrochemical impedance. It was found that the superhydrophobic surfaces showed a better corrosion resistance than that of pure Al and provided promise industrial applications for Al and its alloys.

Also, superhydrophobic aluminum-magnesium alloy was prepared via a simple and low-cost method, and the prepared hierarchical micro/nanostructures demonstrated a high coating coverage rate of 90.0%, resulting in high corrosion protection [111]. Another example, superhydrophobic coatings were prepared via a facile method to protect the steel surfaces from corrosive areas [112].

2.4.2 Oil and water separation

Environmental pollution is a worldwide challenge that occupied the mind of researchers and industries. The pollution produced from different sources contaminates air, water, and soil environment, which affects both the human health and ecological system. Oil plays an essential role in human life and industry. Oil pollution has become a severe challenge due to its high risk of people's livelihoods and the ecological environment [113][114]. Recently the researchers are focusing on special wettable materials such as superhydrophobic surface materials have attracted extraordinary attention due to their environmental friendliness, low energy consumption and simplicity [115].

Superhydrophobic, hybrid, electrospun cellulose acetate nanofibrous mats for oil/water separation was prepared by Arslan et al. [116]. They obtained the superhydrophobic nanofibrous mat by electrospinning techniques. Additionally, the cellulose acetate nanofibers have been adjusted with perfluoro alkoxysilanes for controlling their chemical and physical properties. It was found that the modified hybrid FS/CA-NF nanofibers provide superhydrophobic characteristics with a water contact angle of ~ 155° and proved promising materials for future applications such as oil/water separators and water-resistant nanofibrous structures.

Fu et al. [117] investigated the oil/water separation property of PUF-RC coating cotton fabric. It was found that the separation efficiency remained at greater than 95% even after 20 reuse cycles and showed brilliant durability.

Su et al. [118] fabricated dual-functional superhydrophobic textiles. They reported that the fabricated textile has the characteristics of superhydrophobicity, magnetic responsiveness, excellent chemical stability, adjustable surface morphology, and controllable adhesion. They have also pointed out that the water droplets on the surface firmly adhered even at vertical (90°) and inverted (180°) angles, and this adhesion behavior of the fabricated superhydrophobic textile was successfully applied in oil-water separation.

2.4.3 Self-cleaning surfaces

Self-cleaning surfaces are broadly used in different applications, including industry, military industries, and agriculture. Lately, many approaches have been conducted to produce self-cleaning surfaces. Many superhydrophobic surfaces were utilized to show excellent self-cleaning properties. Kumar et al. [119] synthesized superhydrophobic coatings for aluminum surfaces via the chemical etching method using $HCl+HNO_3$ and HDTMS. The fabricated layer showed a high water contact angle of $162\pm4.2°$ and hysteresis contact angle of $4\pm0.5°$. This coating revealed high thermal, chemical, and mechanical stability as well as excellent superhydrophobic performance after annealing at 200℃ for one hour. Also, the coating displayed an excellent self-cleaning feature, which can be desirable for industrial applications. Latthe et al. [120] prepared superhydrophobic coatings by sprayed suspension hydrophobic silica nanoparticles on different substrates, including motorcycle, building wall, solar cell panel, glass pieces, metal substrates, and fabric shoes. Each coating sample displayed superhydrophobic behavior with a water contact angle around 160 and contact angle hysteresis below 6. An excellent self-cleaning ability and superhydrophobic surfaces were achieved. Sanjay et al. [121] reported the reduction of surface energy of stainless steel substrates by etching SS substrates in sulfuric and

treated with methyltrichlorosilane. The obtained superhydrophobic surface exhibited great self-cleaning and corrosion-resistant properties.

Lu et al. [122] investigated a solution consisting of an ethanolic suspension of perfluorosilane and titanium dioxide nanoparticle. The latter can be sprayed to make a self-cleaning surface. These surfaces showed high water repellency after maintained with some surface modification, such as polishing the surface with sandpapers. Also, the prepared solution can be sprayed on papers, glass, clothes, and steel to enhance the self-cleaning properties of such materials. Zheng et al. [123] fabricated superhydrophobic coating with hierarchical micro-nanostructure, which showed a high water contact angle about $155° \pm 0.5°$ and very low contact angle hysteresis of $3.5° \pm 1.3°$. This coating displayed amazing chemical and mechanical stabilities, as well as an excellent self-cleaning.

2.4.4 Anti-bacterial surfaces

Growth of the biofilms in the environment is one of the main concerns in medical industries, especially in the case of hospital infection. Several superhydrophobic surfaces were used to decrease their adhesion and to kill the biofilm. Wang et al. [124] prepared superhydrophobic silver polydopamine, silver nanoparticles and 1-dodecane thiol surfaces on silicon substrates through facile silver mirror reaction. A high water contact angle was obtained equal to 170° and low contact hysteresis angle about 1°. Also, a long term and broad-spectrum bactericide were utilized with silver nanoparticles to control the bacterial expansion and reach high anti-bacterial activity and limited toxicity.

Privett et al. [125] reported a simple procedure for fluorinated-silica-colloid-superhydrophobic surface synthesis to reduce bacterial adhesion. They found that the combination of micro and nanostructures showed a significant advance, such as

lowering surface energy of fluorinated saline xerogel, which leads to a surface that declines the adhesion of highly pathogenic. Such fluoroalkoxysilane coating surfaces considered great candidates for medical equipment coatings.

Xue et al. [126] constructed superhydrophobic conductive cotton textiles by in situ coating fibers using Ag nanoparticles showed a high antibacterial property. The presence of Ag nanoparticles on the surface exhibits a roughening effect of the fiber structure which enhances the hydrophobic behavior of the cotton textile. Some surface medication was carried out on the cotton textile, such as hydrophobization with HDTM which resulted in a high water contact angle equal $157.3 \pm 1.6°$.

2.4.5 Other applications

In addition to these standard applications of superhydrophobic surfaces, many other applications, including water purification, anti-fogging surfaces, drag reduction, anti-icing surfaces, sensors, and battery manufacture technology, were developed. For example, water treatment technologies become one of the most attracted fields. Superhydrophobic surfaces consist of titania nanoparticles, and semiconductor materials such as ceramic were utilized for the removal of soluble pollutants in wastewater [127]. For anti-fogging applications, superhydrophobic surfaces with high water contact angle can be used to prevent the appearance of vapors on different substrates such as mirrors and glass by monitoring the reaction between substrates and liquid droplets [128]. Moreover, superhydrophobic properties are involved in many sensors to increase their accuracy due to their roughness. Various organic substances with Van der Waals interaction, such as toluene and formaldehyde were used to improve the roughness of superhydrophobic CVD coating [129]. In general, superhydrophobic technology was used to overcome many problems, and since the wettability of the surface played the main concept in the industry, extensive studies and

investigations have been done on different applications. Table 2.2 shows examples of superhydrophobic coatings and their applications.

Table 2.2. Examples of recent publications of superhydrophobic surface and their applications.

Materials	Preparation method	Improved properties	Applications	Ref
A mixture of methyl-modified silica particles and polystyrene	Spin-deposition technique	Anti-corrosion performance Stable self-cleaning	Corrosion resistance Self-cleaning	[130]
Steel surface combining Hydrogen peroxide and an acid	Facile method	Outstanding corrosion resistance and UV-durability	Corrosion resistance, UV-durable	[131]
Graphene-based Composites	Common coating methods	Excellent corrosion resistance (96-78%) properties	Self-cleaning	[112]
Ag nanoparticles coated Al substrate	Chemical etching and anodization	Ag-coating Al substrate prevent corrosion and bacteria absorption	Antibacterial, Anticorrosion	[132]
ZnO nanorod array modified PVDF membrane	Pyrolysis adhesion	Superhydrophobic surface with a water contact angle of 152° and excellent thermal and mechanical stability	Vacuum membrane Distillation, Antifouling	[133]
CuO nanoparticles and hydrophobic silica sol	Spray coating	Reduction in adhesion of bacteria (Escherichia coli. E. Coli) by up to 3.2 log cells/cm^2	Bactericidal property	[134]
Fe_3O_4 @OTS-SiO_2 nanocomposites	Coatings	Lower corrosion current (1.4x 10^{-11} A/cm^2), Lower corrosion rate (ca.1.6x 10^{-7} mm/year), and larger polarization resistance (7.9 x10^4 Mcm^2)	Corrosion resistance	[135]

Materials	Preparation method	Improved properties	Applications	Ref
Transition metal/Metal oxide nanocrystals	In situ growth	Controllable special wettability	Oil/Water separation	[136]
Cu/Ag bimetallic composition	The simple thermal oxidation process	Good antibacterial activity	Antibacterial Activity	[137]

CHAPTER 3: EXPERIMENTAL WORK

3.1 Material

Polystyrene (PS) with average molecular weight (M_W) of 250,000 was supplied with a specific density of 1.05 g/cm^3 by Sigma-Aldrich (Taufkirchen, Germany). Nickel oxide (NiO) nanopowder with particle size < 50 nm, which used to improve the hydrophobicity of polystyrene, was also obtained from Sigma-Aldrich. The solvents used, N, N-Dimethylacitamide (DMAC), and Tetrahydrofuran (THF), were purchased from BDH Chemicals (Doha, Qatar) as volatile and nonvolatile solvents respectively.

3.2. Sample preparation

3.2.1 Synthesis of PS-NiO superhydrophobic coating

A 3g of polystyrene was dissolved in a 50 ml mixture consisting of 70 wt% DMAC and 30 wt% THF and stirred overnight at 30 ℃ to get a sufficiently homogenous solution with the required viscosity for electrospinning. At the same time, different concentrations of NiO nanoparticle were dissolved in 25 ml of a mixture consisting of the same ratio of solvents and kept under steering condition overnight to get well dissolved of the nanoparticles. Then, the NiO nanoparticle solution was gradually added to PS solution and stirred for 3 hours at 50 ℃. The PS and different NiO concentrations prepared are shown in Table 3.1. Aluminum substrates with 3 x 3cm^2 size, which were used as collectors and coated with PS/NiO superhydrophobic coating, were smoothly polished on Grinder polisher (Metko FORCIPOIV, Bursa, Turkey) using a 500 sandpaper and washed with distilled water and dried.

Table 3.1. compositions and electrospinning parameters for pure PS and PS/NiO nanocomposite coatings

Exp. Code	PS (g)	NiO (g)	Potential (kV)	Flow rate ($mL.h^{-1}$)
PS	3	-	18	1.5
PSNI-1	3	0.1	18	1.5
PSNI-2	3	0.15	18	1.5
PSNI-3	3	0.2	18	1.5

3.2.2 Electrospinning technique

The electrospinning piece of equipment is composed of four main parts as shown in Figure 3.1. The injection pump that adjust the solution flow automatically, the injection syringe, which contains the polymer solution, the power supply with high voltage, and the sample collector. The polymer solution must be well dissolved before being electrospun.

Figure 3.1. Electrospinning equipment

The electrospinning device has been used to fabricate PS/NiO superhydrophobic coating. The syringe pump was fixed vertically, and an electric field was obtained by a high voltage supply. The homogenous PS/NiO nanocomposite solution was transferred by syringe to be sprayed by the needle. The optimum distance used to get the beaded fibers was 15 cm from the tip of the needle to the substrates. The needle used to spin the nanocomposite solution has a cross-sectional diameter of 0.7 mm. The electrospinning flow rate was 1.5 mL h^{-1}, the applied voltage was 18 kV, and the operation temperature was ambient temperature 25 ℃. These experiments were operated at relatively low applied voltage due to the agglomeration of the NiO nanoparticles were observed as the applied voltage increase to 20 kV and above.

Figure 3.2. Coatings samples prepared via electrospinning technique

3.3 Characterization Methods

3.3.1 Scanning Electron Microscopy (SEM) and EDX

High field emission scanning electron microscopy HFESEM (FEI NOVA NANOSEM 450, Hillsboro, OR, USA) attached to an energy dispersion X-ray analysis unit EDX shown in Figure 3.3 was used to study the morphology of PS/NiO nanocomposite

superhydrophobic coating at different magnitude 2000, 5000, and 10,000x. To get high-resolution images the samples were placed in a distance between the sample and the source of electrons of 10 nm. The machine was operated at a high voltage of 12.5 kV. Then, the electrons were transferred via high-speed beams and hit the sample. The reflected electrons were detected by SEM, and the absorbed ones interact with the specimen to provide a semi-quantitative elemental analysis by EDX. ImageJ software was used to calculate the average fiber diameters of the resulted SEM images for both polystyrene and polystyrene/nickel oxide nanocomposite superhydrophobic material.

Figure 3.3. High Field Emmission Scanning Electron Microscope

3.3.2 Atomic Force Microscopy (AFM)

Atomic force microscopy was performed using an MFP-3D, Asylum Research, Santa Barbara, CA, USA, shown in Figure 3.4. AFM measurements were carried out using silicon tip, which has a radius of 10 nm over a resonance frequency of 70 kHz in

addition to a spring with a constant of 2 Nm^{-1}, which was used for the non-contact tapping mode in air. The AFM device was usually used to study the degree of roughness of materials or surfaces. The obtained AFM images consist of signals which have been represented along Z distance of motion per x, y points on the scanning raster. Then, those signals which represent several measurements were collected and read as a voltage points in MFP-3D system.

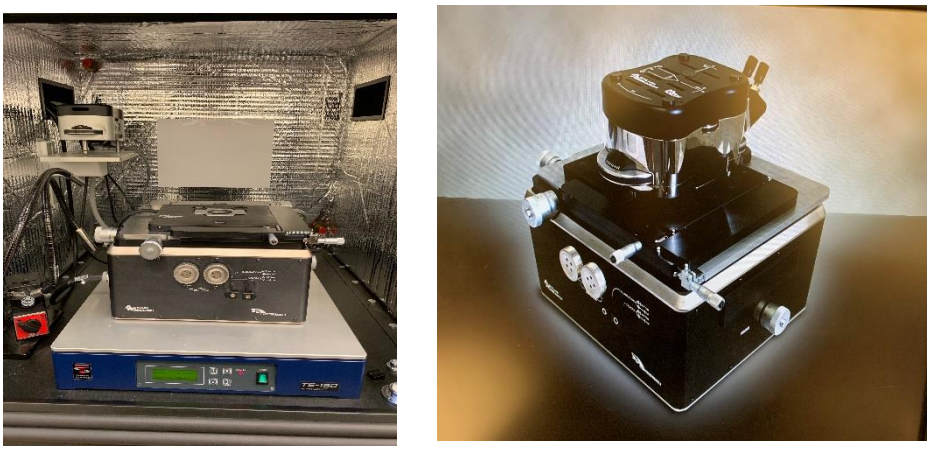

Figure 3.4. Atomic Force Microscopy ((MFP-3D, Asylum Reaerch)

3.3.3 Fourier Transform Infrared Spectroscopy (FTIR)

Fourier transform infrared was measured using (PerkinElmer Spectrum 400 FTIR, PerkinElmer, Waltham, MA, USA) shown in Figure 3.5. The FTIR spectra were recorded of the sample within a wavenumber range of 400-4000 cm^{-1} and display a resolution of 2 cm^{-1}. The principle is that when the infrared radiation passes through PS/NiO SH coating, the coating absorbs some of the radiation and release some. The result gives the molecular identification of the sample. Also FTIR analysis was used as

fingerprint to identify organic, polymeric and some inorganic materials.

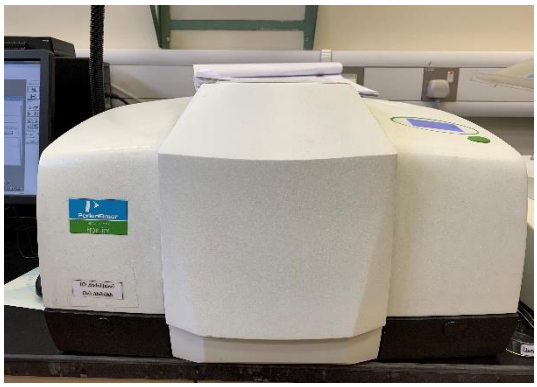

Figure 3.5. FTIR instrument model: PerkinElmer Frontier

3.3.4 X-Ray Diffraction (XRD)

X-ray diffraction analysis was performed using X-ray Diffractometer (Empyrean, Panalytical, UK) shown in Figure 3.6. XRD device made of three main elements, including: cathodic ray tube, a sample holder, and an X-ray detector. In the cathodic ray tube the X-rays are generated where a filament is heated to produce electrons that accelerate toward the anode by applying a high voltage of 45 kV. When the electrons gain enough energy to hit the inner shell of the target material an X-ray of 1.54 nm wavelength is produced. In the holder section, a divergent slit of 0.19 mm focusses the X-ray on the sample to ensure more area of the sample is exposed to get the intensity of the scattered ray. This intensity is measured by the rotation detector. Also, the aligned geometry rotation at an angle of 2θ is maintained by the goniometer at the center of the device.

Figure 3.6 .The PAN analytical X-Ray diffractometer

3.3.5 Contact Angle Measurement

Water contact angles were measured using an optical contact angle measuring system (OCA 35, Dataphysics Instruments, Filderstadt, Germany) shown in Figure 3.7. The device is attached to an automatic image recognition and computation software, which are used to calculate liquid-solid contact angles and surface energy. Water droplets of 4 **µL** were moved slightly out of the syringe and placed on the surface of the sample. The equilibrium contact angle and roll-off angle were found using the provided software. The roll-off angle known as the sliding angle (AS) can be calculated by slightly incline the substrate holder until the water droplet was noticed to move. At this point, two contact angles were recorded, including: advancing contact angle (ACA) and receding contact angle (RCA). Water contact angles were measured at three different positions at the surface of each sample.

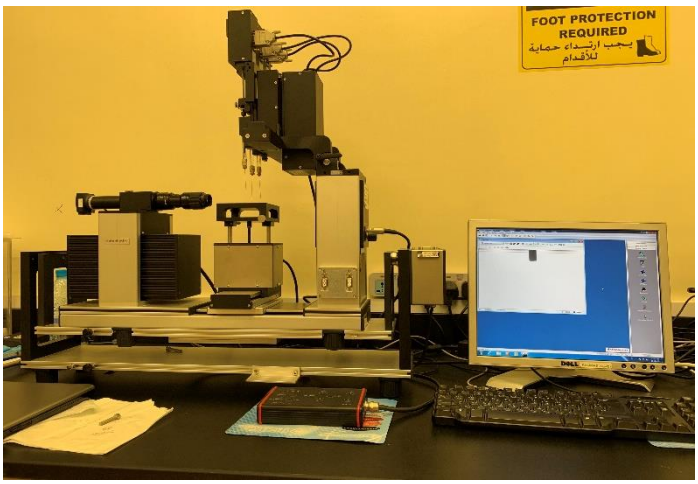

Figure 3.7. Optical Contact angle Measuring System.

3.3.6 Differential Scanning Calorimetry (DSC)

Differential scanning calorimetry (DSC) is used to measure the heat flow between the sample and the reference as a function of temperature and time in controlled atmosphere. DSC analysis was conducted using a differential scanning calorimeter (DSC 8500, PerkinElmer, US) shown in Figure 3.8. DSC was widely used for thermal characterization of materials, which provides several pieces of information about the thermal behavior of the material such as melting and crystallization temperature, heat of fusion, heat capacity, and heat of reaction. Different samples weigh 7.31mg, 6.75, 6.18, and 6.09 mg for PS, PSNI-1, PSNI-2, and PSNI-3, respectively were placed in the aluminum pan to be measured parallel with an empty pan considered as a reference. The temperature range of the testing sample was from -30 ℃ to 250 ℃ with scan rate of 10 ℃/min. Three steps were performed consisting of two heating steps to calculate the specific enthalpy of melting (ΔH_m) after eliminating the thermal history of the sample, and one cooling step.

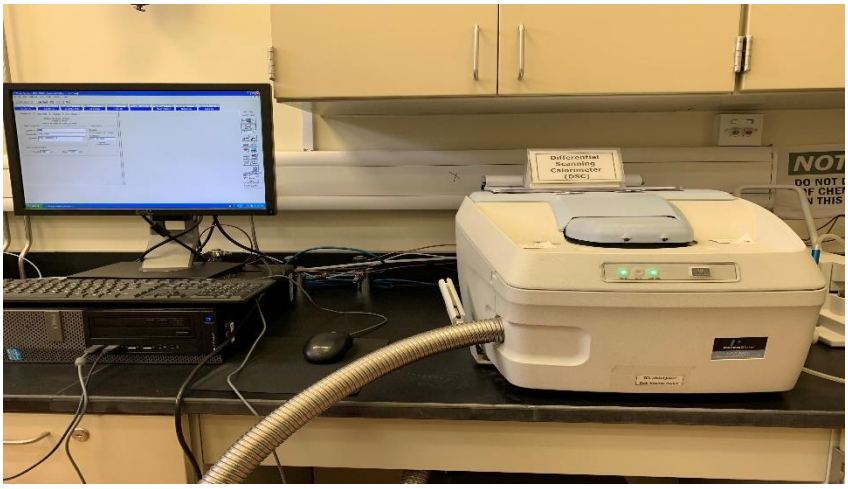

Figure 3.8. Differential Scanning Calorimeter (DSC 8500 Perkin Elmer)

3.3.7 Thermogravimetric Analysis (TGA)

Thermogravimetric analysis measurements were performed using (4000 Perkin Elmer Pyris system) shown in Figure 3.9. (TGA) was used to find the weight percent loss of a sample as a function of temperature in a controlled atmosphere. Usually a plot of a mass percentage versus temperature indicates the thermal decomposition of the sample. The weight of the sample must be between 5-10 mg. A small alumina crucible (ceramic) was used as a container to place the sample in the device. The device is attached to computation software to adjust the temperature and record the spectra of the measurements. The temperature range applied in this test was from ambient room temperature 25 ℃ to 600 ^{0}C at a heating rate of 10 ^{0}℃ min^{-1}. The experiments were conducted in the presence of continuous nitrogen flow rate. The weight of each sample was around 8 mg. TGA can be used to identify the thermal stability, oxidative stability, decomposition kinetics, and the lifetime of the materials, and also it can indicate any

effect of the reactive or corrosive atmosphere on the material.

Figure 3.9. Thermogravimetric analysis device (TGA, 4000 Perkin Elmer)

3.3.8 Electrochemical impedance spectroscopy (EIS)

Electrochemical impedance spectroscopy is one of the most powerful techniques used to determine the corrosion resistance of the materials. EIS is an easy and qualitative technique used to measure the performance of anti-corrosion materials. Gamry Reference 3000 potentiostat (Warminster, PA, USA) shown in Figure 3.10 was utilized to measure the electrochemical performance of PS/NiO superhydrophobic nanocomposite coatings. Gamry Reference 3000 potentiostat is used along with an electrochemical cell that consists of three electrodes: saturated calomel reference electrode (SCE), the working electrode (the Al substrate coated with or without PS/NiO) and the counter electrode which is used as graphite. The coating samples with surface area of 0.785 cm^2 were exposed to 3.5 wt% NaCl solution. EIS measurements were carried out at an open circuit with a wave amplitude of 10 mV over a frequency range of 0.01 Hz to 100 kHz at room temperature. Before conducting EIS

measurements, the sample was immersed 30 min in 3.5 wt% NaCl solution to reach the steady-state and set the open circuit potential. EIS data were analyzed using Gamry Echem Analyst software (Version 7.06, Gamry, Warminster, PA, USA).

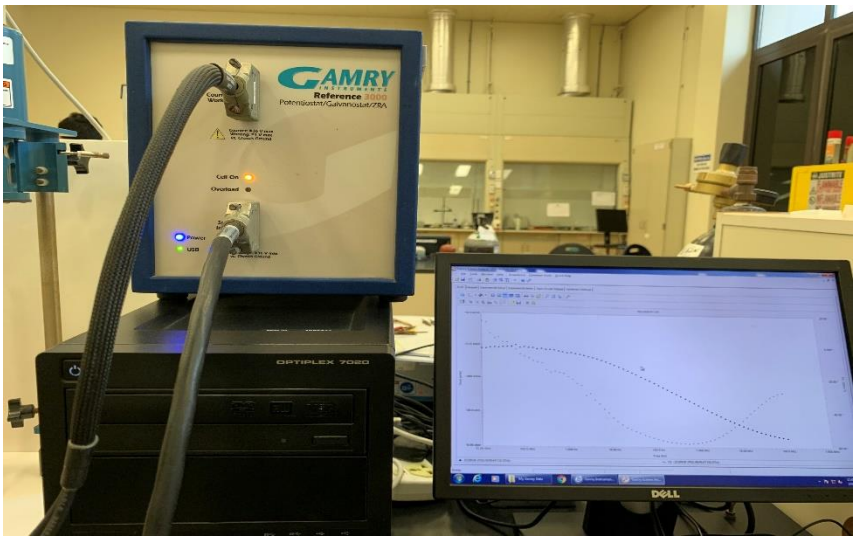

Figure 3.10. Power station instrument model: GAMRY refrance 3000

CHAPTER 4: RESULTS AND DISCUSSION

4.1. Structure and Morphology

4.1.1. Scanning Electron Microscopy (SEM)

The morphology of the electrospun PS and PS/NiO nanocomposite superhydrophobic coatings at different concentrations of NiO nanoparticle was observed by the scanning electron images shown in Figure 4.1. SEM micrographs show several morphologies, including fibers with diameters ranging between 100 nm to 250 nm and a large number of beads. These beads may be obtained because of the low polystyrene concentrations or the operating parameters of the electrospinning [138]. The neat PS morphology shown in image (a) proves the formation of beaded fibers structure. Actually, under the tested conditions, the creation of spindle beaded fibers has two reasons: first, resulted from the low applied voltages 18 kV for electrospun process as well as the fast stretching through the charged jet [20][138]. Second, low PS concentration leads to a significant decrease in the elasticity needed to provide the required resistance to overcome the elongation caused by the electrostatic force which produces a large number of beads [139]. In general, there are three forces accountable for the formation of the beads: coulombic, viscoelastic and the surface tension forces in addition to the stretching of the charged jet during the electrospun process. A smooth fibers can be generated by increasing the applied voltage more than 25kV or increasing polymer concentration [139][88].

The presence of NiO nanoparticles impacts the surface morphology of the electrospun polystyrene displayed in Figure 4.1 (b, c, and d). As clearly noticed from these figures, there are different sizes of beaded fibers and small fiber diameters, however, the addition of nanoparticles does not change the surface morphology of the electrospun polymers.

The beads-on-fiber electrospun coating is desirable since the beads-structure and nanofiber structure together contribute to the roughness of the coating and increase the trapped air, which enhances the hydrophobicity of the materials [138].

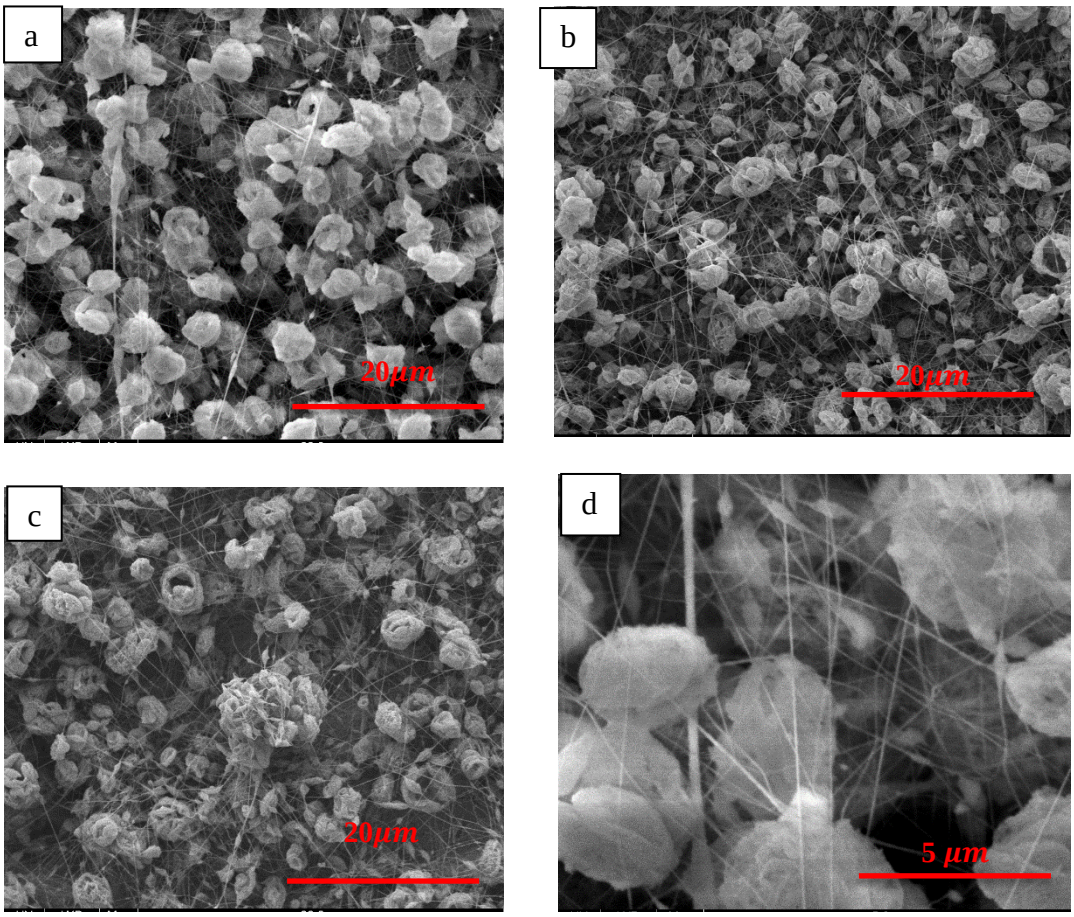

Figure 4.1. SEM images of electrospun PS and PS/NiO nanocomposite superhydrophobic coating for (a) PS, (b) PSNI-1, (c) PSNI-2, and (d) PSNI-3 at 10000x

Table 4.1. Summarizes the average fiber diameters of the prepared electrospun polystyrene and polystyrene/NiO nanocomposite superhydrophobic coating. There is a notable difference in the calculated fibers' diameters of the polystyrene and PS/NiO nanocomposite as the concentration of NiO nanoparticles changes. All the experiments

were conducted at constant electrospinning parameters, while the concentration of the NiO nanoparticle was varied to get the optimum results. Also, PS concentration was fixed at 4 wt% to achieve the desired ratio corresponding to the NiO nanoparticle. The concentration of PS was little low, which produces relatively large fiber diameters (around 240 $\pm$ 28 nm). However, based on literature, if the concentration of the polymeric solution increases, the solution viscosity increase and becomes easier to elongate [84]. Also, by increasing the concentration of the polystyrene the viscoelastic force stops the electrospinning jet from being stretched by the constant columbic force, which produces large fiber diameters and beads [20].

On the other hand, the addition of NiO nanoparticle caused a considerable reduction in the average diameters of the PS/NiO nanocomposite fibers compared to pure PS. It was clearly observed that there was a significant decrease in the average fiber diameters from 240 $\pm$ 28 for pure PS to 168 $\pm$ 14 nm in PS/NiO (PSNI-3). Hence, as the concentration of NiO nanoparticle increased from 0.4 wt% (PSNI-1) to 0.8 wt% (PSNI-3), a further reduction in the fiber diameter from 176 $\pm$ 29 to 168 $\pm$ 14 nm was noticed. Moreover, The SEM-EDX mapping micrographs and spectra of PS/NiO nanocomposite SHCs, shown in Figure 4.2 confirm, the presence of the Ni and O atoms on the beaded fibers structure. Also, EDX spectra of the PS after the addition of NiO show the percentage of Ni and O is about 4.61 and 4.84 wt%, respectively on the fabricated coatings [140].

Table 4.1. The average diameter of the nanofibers of Pure PS and PS/NiO nanocomposite coatings

Sample	Average Fiber Diameter (nm)
PS	240 ± 28
PSNI-1	176 ± 29
PSNI-2	172 ± 36
PSNI-3	168 ± 14

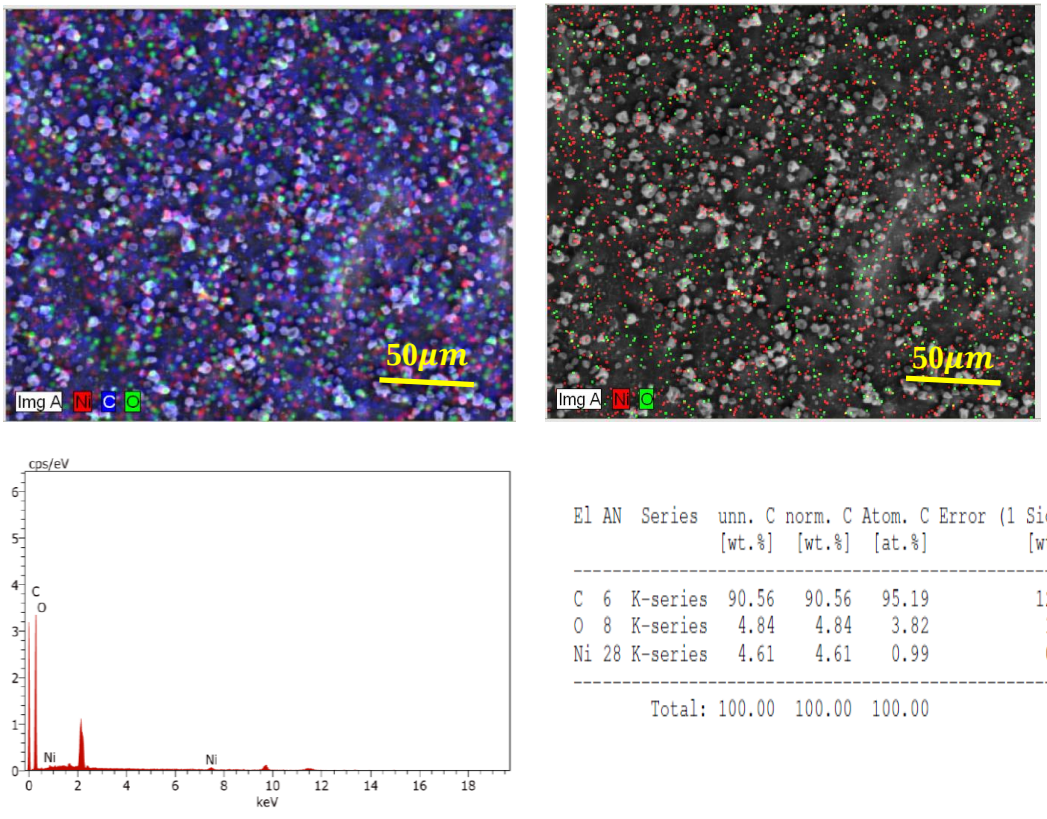

Figure. 4.2 SEM-EDX mapping micrographs and spectra of PS and PS/NiO nanocomposite SHCs

4.1.2 Contact Angle Measurement

Figure 4.3 shows the wettability of the electrospun PS and PS/NiO nanocomposite superhydrophobic coatings. The water contact angles of the prepared coatings were investigated through the sessile droplet method at room temperature. Table 4.2 demonstrates the measured water contact angles and sliding angles for both PS and PS/NiO nanocomposite coatings. The water contact angles were measured for polystyrene before and after the addition of NiO nanoparticle at PS concertation of 4 wt%. Image (a) in Figure 4.3 shows that the WCA of pure polystyrene was $146° \pm 2°$. The WCA of PS coating reveals the hydrophobic nature of the polymer. However, the addition of NiO nanoparticles to PS enhances the hydrophobicity of the fabricated coating. The highest water contact angle of PS/NiO nanocomposite coatings was $155° \pm 1°$ for PSNI-2, and the lowest contact angle was $150° \pm 2°$ for PSNI-3. The water contact angle increase with increasing the amount of NiO nanoparticle until a certain limit; beyond which, the WCA declines due to the aggregation of the NiO nanoparticles [141].

Cassie-Baxter model was used to calculate the static contact angles based on the following equations [142]:

$$\cos\theta_{CB} = f_1 \cos\theta_{\gamma} - f_2 \qquad (4.1)$$

Where θ_{CB} is the contact angle of the (PS/NiO) nanocomposite coating, θ_{γ} is the smooth (PS) surface water contact angle, and f_1 and f_2 are the area fraction of the heterogeneous surface which $f_1 + f_2 = 1$.

Cassie-Baxter's ideal hypothesis stated that the water droplet is hanged on the rough surface causing a heterogeneous structure composed of air and solid [143]. This model was selected to evaluate the WCA of the Nano composition coating (PS/NiO). The calculated θ_{CB} was $153°$, $155° \pm 1°$ and $150° \pm 2°$ for PSNI-1, PSNI-2 and PSNI-

3 respectively, and the measured values of θ_γ for PS coating was $146° \pm 2°$. Also, the calculated values of f_2 were 0.41, 0.48 and 0.43. This result indicates that air fills around 41%, 48%, and 43% of the solid-liquid contact area for PSNI-1, PSNI-2 and PSNI-3 nanocomposite superhydrophobic coating, respectively. In fact, one of the fundamentals behind the superhydrophobic phenomenon of the PS/NiO composite coating is the enhancement of hierarchical structure of the surface, which resulted from the formed heterogeneous surface as confirmed by the calculated parameters.

The contact angles hysteresis (CAH) were measured for both polystyrene and polystyrene/NiO nanocomposite SHC shown in Table 4.2. The water contact angle hysteresis usually used as a tool to indicate the stickiness of the surfaces. The measured CAH of pure polystyrene coating nanoparticles was $25° \pm 3°$. Polystyrene CAH was relatively high which verifies that such prepared surfaces are not superhydrophobic [144]. However, the CAHs of polystyrene coatings after the addition of NiO nanoparticles PS/NiO markedly decreases to $8° \pm 2°$, $5° \pm 3°$, $12° \pm 2°$ for PSNI-1, PSNI-2, and PSNI-3 respectively. Accordingly, these results evidenced that there is a weak adhesion force between the polystyrene/NiO superhydrophobic coating and the water droplet, which leads to a fast slide of the droplets on the sample surfaces [145]. Also, the obtained results are in agreement with literature and prove that the greatest water contact angle (WCA) displays the lowest contact angle hysteresis (CAH), which is (PSNI-2) the best superhydrophobic coating found using PS polymer and NiO nanoparticles. In contrast, high water contact angle not always indicates a low contact angle hysteresis because of the influence of chemical heterogeneity of the material [144].

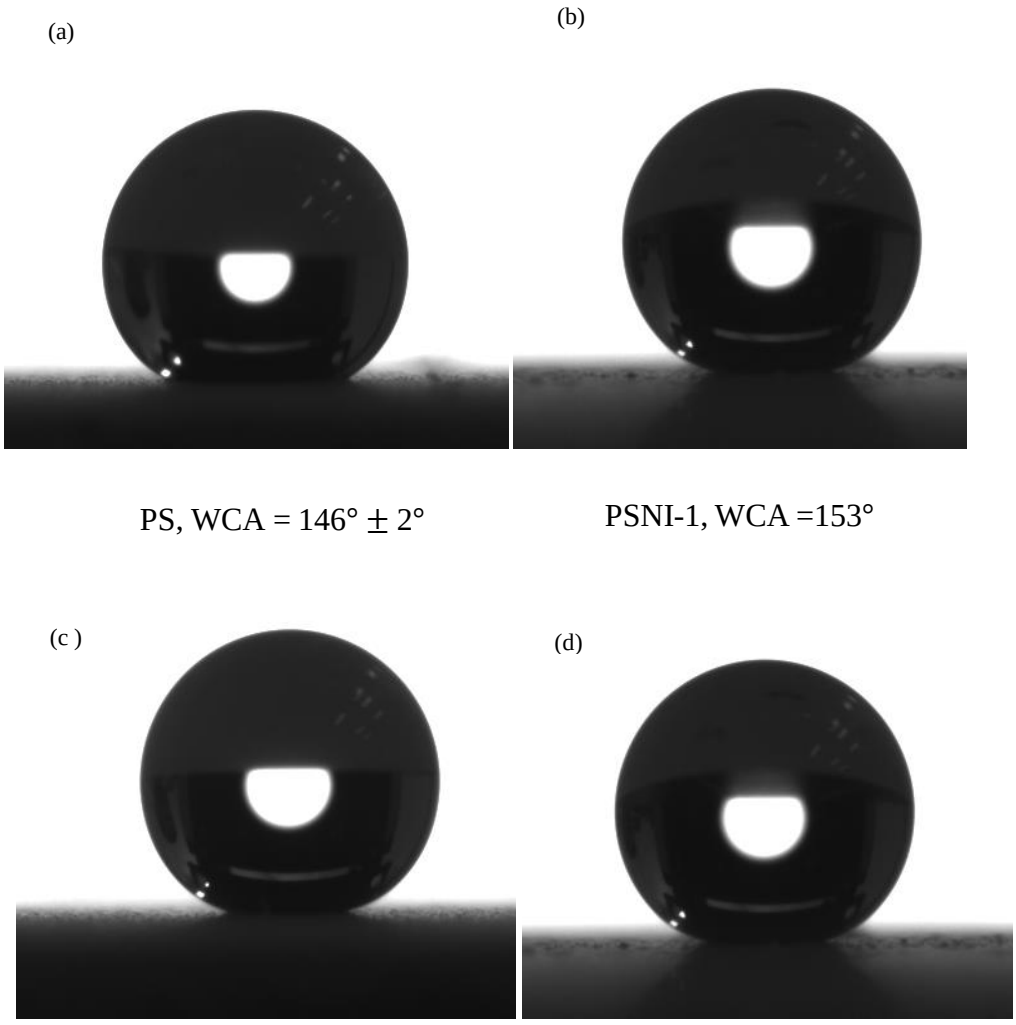

Figure 4.3. water contact angle measurements for pure PS and PS/NiO nanocomposite SHCs

Table 4.2. WCA and WCAH of the prepared PS and PS/NiO nanocomposite SHCs.

Sample	Water Contact Angle (WCA)	Water Contact angle Hysteresis (WCAH)
PS	$146° \pm 2°$	$25° \pm 3°$
PSNI-1	$153° \pm 2°$	$8° \pm 2°$
PSNI-2	$155° \pm 1°$	$5° \pm 3°$
PSNI-3	$150° \pm 2°$	$12° \pm 2°$

4.1.3. Atomic Force Microscopy (AFM)

AFM images were performed to study the surface roughness and surface topography of both pure PS and PS/NiO nanocomposite SHCs as illustrated by Figure 4.4. It is obviously shown that the polystyrene surface is quite smooth except small bumps, which may be resulted from the structure of the beaded fibers. The roughness value (R_{rms}) of pure PS coating is found to be about 18.49 nm. However, the addition of NiO nanoparticle rapidly increases the degree of surface roughness of the PS coating. The surface roughness of the PS/NiO nanocomposite SHC increases with the increase of NiO nanoparticle concentration up to a certain limit; beyond that limit R_{rms} values slightly decline [146]. The R_{rms} value of the prepare coatings is found to be equal 24.717, 31.856, and 38.290 nm for PSNI-1, PSNI-2 and, PSNI-3 respectively. This result demonstrates that the higher the concentration of NiO nanoparticles, the higher the surface roughness of the coating will be. In general, AFM measurements draw attention to the impact of the composition ratio of PS to NiO nanoparticle on the degree of roughness of the prepared coatings. It worth mentioning that the formed microbeads and nanofiber structures increase the surface roughness of the coatings. However, the high rough surface not necessarily display the greater WCA and best hydrophobicity

properties since there are several factors can influence the hydrophobicity degree of the materials.

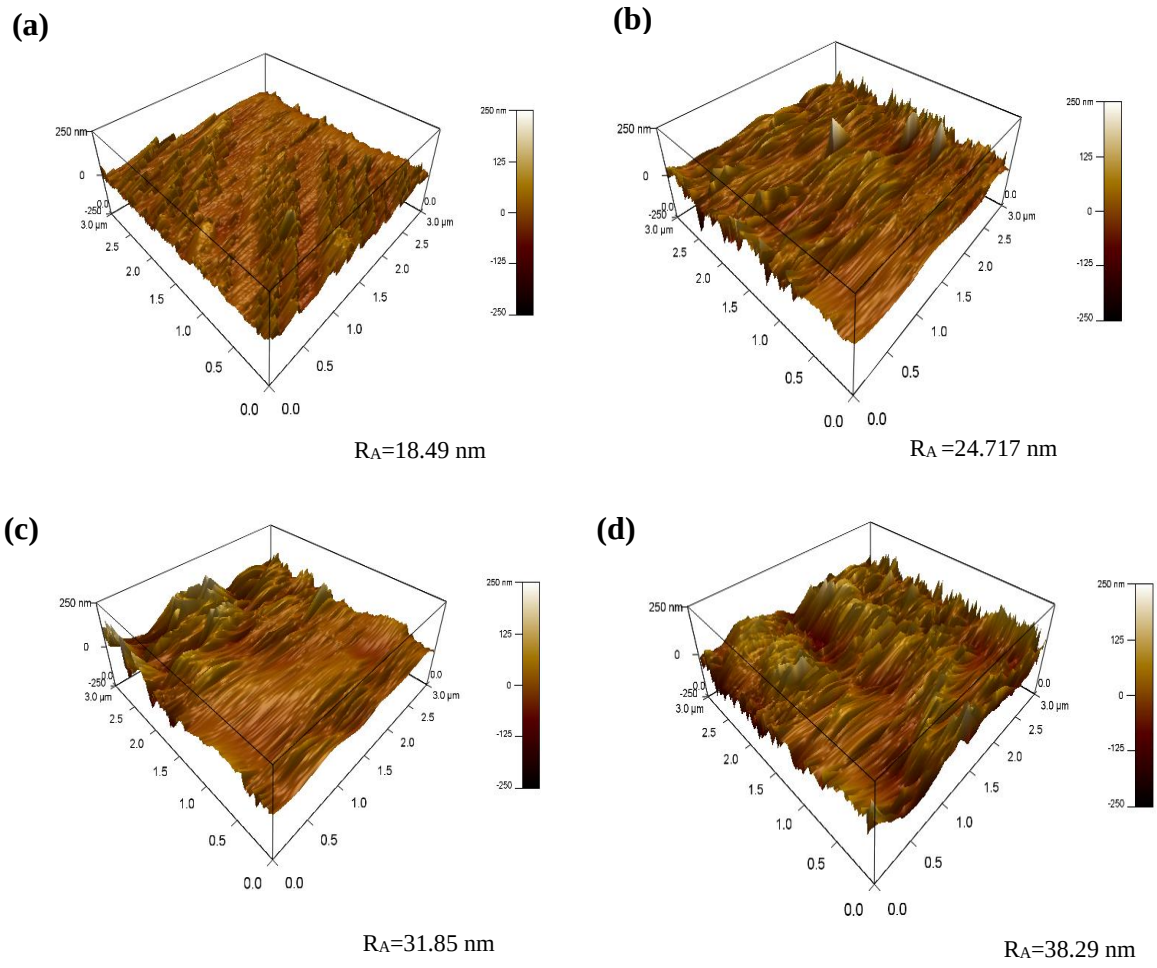

R_A=18.49 nm

R_A =24.717 nm

R_A=31.85 nm

R_A=38.29 nm

Figure 4.4. AFM images of surface of (a) PS, (b) PSNI-1, (c) PSNI-2, and (d) PSNI-3 with surface area of 1 μm^2.

4.1.4. Fourier Transformation Infrared Spectroscopy (FTIR)

The structural properties and the functional groups of the electrospun PS and PS/NiO coatings were recorded by an FTIR spectrophotometer. FTIR spectra of pure PS and PS/NiO nanocomposite coating at various concentrations of NiO nanoparticle shown

in Figure 4.5. The spectra of PS coating before and after the addition of NiO nanoparticle are similar. Actually, there are no significant changes noticed after the addition of NiO nanoparticles. This observation might be due to the small amount of the NiO nanoparticle present compared to the large amount of PS. In the FTIR spectra a transmission band is observed around 3100 cm^{-1}, which assigned to O-H bond stretching of water molecules on the PS surface. While the wide absorption band at a wavenumber of 700 cm^{-1} corresponded to the bonding stretch of Ni-O bond [147]. The FTIR shows the same spectra over the region of 1000 cm^{1} to 3000 cm^{-1} for both PS and PS/NiO nanocomposite coatings. The observed bands refer to functional groups. For instance, the peaks that occurred at about 2800 cm^{-1} and 2900 cm^{-1} are assigned to the bonding vibration of C-H functional group of polystyrene [148]. As well as the weak peaks noticed at 800 cm^{-1} and 1300 cm^{-1} refer to the C-H stretching vibration of the $–CH_2$ functional group of polystyrene [149]. Two peaks at 1400 cm^{-1} and 1500 cm^{-1} are corresponding to C-C stretching in the aromatic ring. Also the peaks observed at 1665 cm^{-1} to 1947 cm^{-1} are corresponding to monosubstituted C-C aromatic aromatic rings [150]. Finally, there were no new peaks and bands noticed after the addition of NiO nanoparticles to polystyrene. These results confirm that the NiO nanoparticle only exists physically with polystyrene and did not influence the chemical structure of the polymer.

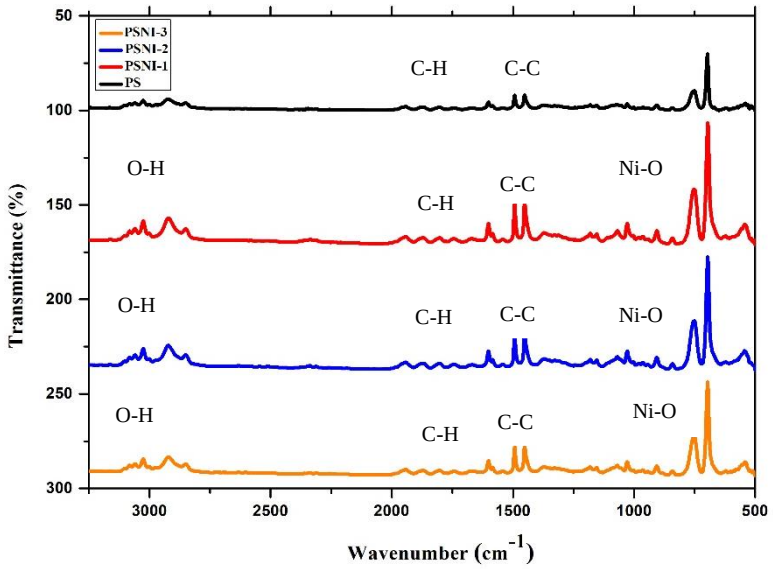

Figure 4.5. FTIR spectra for pure PS and PS/NiO nanocomposite superhydrophobic coatings

4.1.5. X-Ray Diffraction

X-ray diffraction patterns of polystyrene and polystyrene/NiO nanocomposites shown in Figure 4.6 to study the crystal structure of PS/NiO superhydrophobic coating with different concentrations of NiO nanoparticle. The measured peaks in the pattern show four diffraction peaks at average 2θ equal 19.5°, 37°, 43°, and 62°. The last three peaks are recognized with the diffraction line of crystalline plates of [111], [200], and [220] of the cubic phase of NiO, respectively [150][151] [148]. In addition, there was amorphous peak observed at 2θ of 19° which corresponds to the presence of the periodicity parallel to the polymeric chain in polystyrene [152]. It is clearly noticed that the characteristic peaks of pure polystyrene have not changed after the addition of NiO nanoparticles except small peaks were observed and get sharper as the concentration of NiO nanoparticle increased from 0.1 g (PSNI-1) to 0.2 g (PSNI-3). These peaks noticed at 2θ of 37°, 43° and 62° are referred to the nickel oxide nanoparticle which has crystalline ceramic structure. Therefore, based on literature it was confirmed that the

NiO has a face-centered cubic crystal structure with lattice parameter of a = 0.419 nm [150]. Also, The average NiO nanoparticles size was calculated according to Scherrer's equation (4.2) [153] and was found to be equal 44.56 nm.

$$l = \frac{k\lambda}{\beta \cos\theta} \qquad (4.2)$$

Where, l is the average nanoparticle size, k is the phase factor, λ is the wavelength ($\lambda = 0.154\ nm$), $\beta\ is\ the$ full width at half maximum and θ is the angle at maximum intensity.

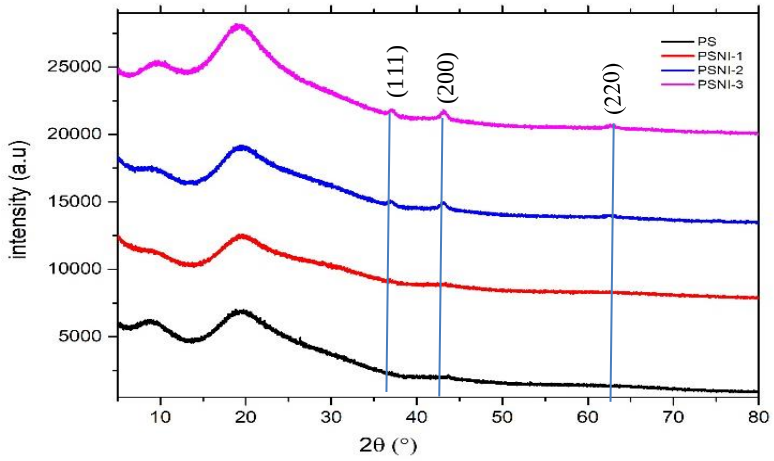

Figure 4.6. X-Ray diffraction pattern of polystyrene/NiO nanocomposite superhydrophobic coatings

4.2. Thermal Properties

4.2.1 Differential scanning calorimetry (DSC)

The deferential scanning calorimetry analysis was done to study thermal behaviors of electrospun PS and PS/NiO nanocomposite coatings. Figure 4.7 displays melting and crystallization curves of PS and PS/NiO obtained from the second heating step and first cooling step by DSC. The temperature of DSC measurements was raised from -30℃ to

250℃ at a scan speed of 10 ℃ min^{-1}. The glass transition temperature is observed at 107 ℃ for bothe polystyrene and polystyrene/NiO nanocomposite. In fact, glass transition phenomenon is time and temperature-dependent, so glass transition temperature changes with the scan speed [154]. The existence of NiO nanoparticles did not cause any change in the temperature of glass transition of polystyrene. Moreover, PS glass transition temperature mainly depends on the average molecular wieght [155]. The melting temperature of PS before and after the addition of NiO nanoparticles is exactly same, which was around 110℃ as noticed from the melting curve of composites shown in Figure 4.7(a). Also, the crystallization behavior of polystyrene and polystyrene/NiO nanocomposites is identical; no cold crystaline peak is observed, as shown in Figure 4.7 (b). Therefore, polystyrene under these conditions is a morphous polymer evidenced by the degree of crystallization measured from Equation 4.2. The enhancement of the glass transiton temperature, melting and crystallization temperature of PS were tricky because of the rigidity of phenyl rings [150]. Accordingly, Esmaiel et al. reported that the presence of NiO nanoparticle reduces the mobility of the polymeric chain, which leads to an increase in the crystallinity of the polymer with increasing regularity, which causes an increase in the glass transition temperature of the polymer [150]. While this work showed that there was no effect of the NiO nanoparticle on the PS thermal properties, this could be due to the small amount of the NiO nanoparticles used compared to PS. The degree of crystallinity of the fabricated coatings was evaluated using the following equation:

$$X_{cry} = \frac{\Delta H_m}{\Delta H^{\circ}} \times 100 \qquad (4.3)$$

Where, ΔH_m is the melting enthalpy of the electrospun polystyrene and PS/NiO SHCs and ΔH° is the melting enthalpy of 100 crystalline polystyrene equal 53.2 J g^{-1} [156]. The calculated values of T_g, ΔH_m and X_{cry} for PS and PS/NiO nanocomposite super-

hydrophobic coatings are summarized in Table 4.3.

Table 4.3. DSC data for pure PS and PS/NiO nanocomposite superhydrophobic coatings.

Sample	T_g(℃)	ΔH_m(J/g)	X_{cry} (%)
PS	107.5	2.159	4.06
PSNI-1	107.7	1.664	3.13
PSNI-2	108.2	1.3.61	2.55
PSNI-3	107.48	1.412	2.65

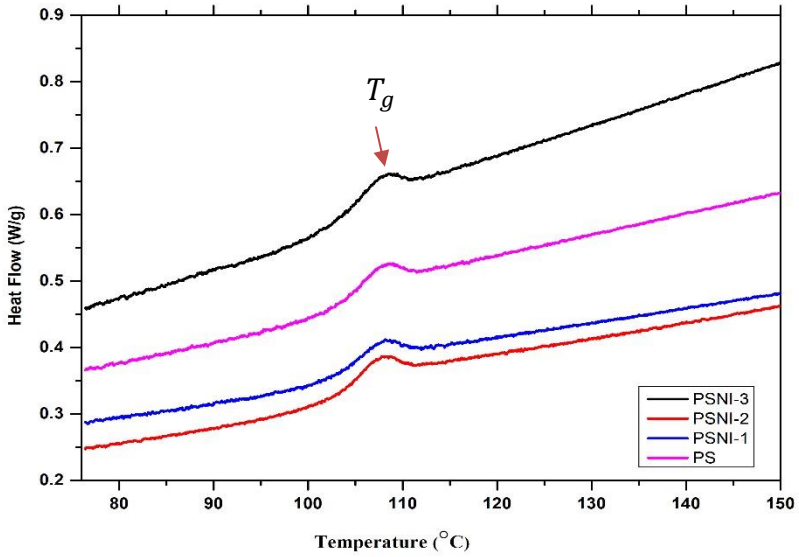

Figure 4.7. DSC analysis for polystyrene and polystyrene/NiO nanocomposites (Heating curve)

4.2.2. Thermogravimetric analysis (TGA)

In order to study the thermal degradation that occurred during heat treatment of the PS and PS/NiO nanocomposite superhydrophobic coating samples, TGA analysis was conducted over temperature range from 25℃ to 600℃ in the presence of N_2 shown in Figure 4.8. The calculated temperatures corresponded to the percent of weight loss

are listed in Table 4.4. The thermal decomposition of the prepared coatings was slightly varied for PS before and after the addition of NiO nanoparticle. Pure PS degrades at temperature around 350℃ [157]. The onset decomposition temperature (T_o) and the temperature for 10% decomposition ($T_{10\%}$) increase with increasing the concentration of NiO nanoparticles. These degradation temperatures are shifted by 30 ℃ to higher temperatures in the presence of NiO nanoparticle compared to pure PS, which are 354, 375, and 375 ℃ for PS, PSNI-1, and both PSNI-2 and PSNI-3 coatings, respectively [84]. As clearly seen, this behavior was kept through the thermal decomposition of the samples as the concentration of NiO nanoparticle increased. Also, it was found that there was a rapid weight loss from 10 to 90% of PS and PS/NiO nanocomposite existed in the temperature range of 330-400 ℃. Accordingly, these observations confirm that the thermal stability of polystyrene is increased by increasing NiO nanoparticle concentration as a result of the limitation of mobility of the polymer chain [158]. The reaction was completed by 440, 450 and 470 for PS and PSNI-1, PSNI-2 and PSN-3 respectively.

Table 4.4. TGA data of PS and PS/NiO nanocomposite Superhydrophobic coatings

Sample	T_{onset} (℃)	$T_{5\%}$ (℃)	$T_{10\%}$ (℃)	$T_{50\%}$ (℃)	T_0(℃)
PS	354.78	353.6	369.92	405.52	440
PSNI-1	371.02	371.42	385.22	412.63	450
PSNI-2	375.42	376.3	388.37	415.05	470
PSNI-3	375.42	375.51	387.67	417.42	470

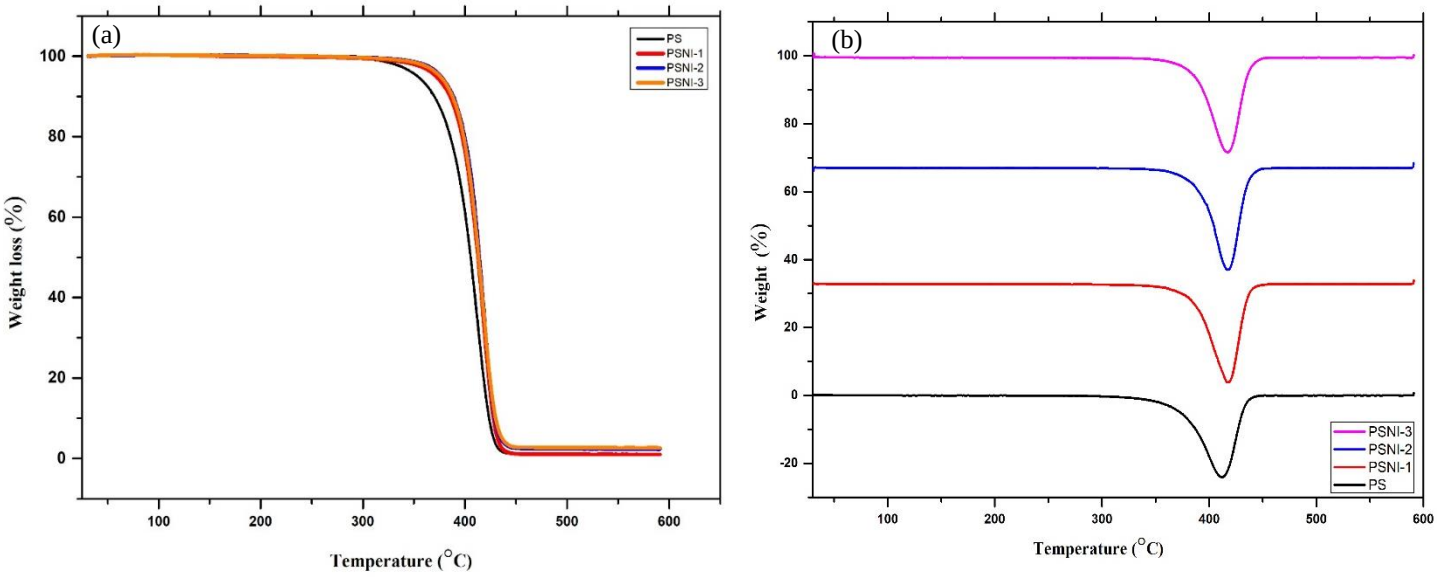

Figure 4.8. Thermogravimetric Analysis for pure PS and PS/NiO nanocomposite Super hydrophobic coatings (a) Linear TGA (b) DerivativeTGA.

4.3 Electrochemical Impedance Spectroscopy (EIS)

A complete study of corrosion resistance of PS and PS/NiO superhydrophobic coatings is achieved by electrochemical impedance spectroscopy shown in Figure 4.10, and Figure 4.11. The variation of the impedance with frequency can be displayed by two techniques: Nyquist method which plots $Z_{imaginary}$ versus Z_{real} for different values of frequency (f), and Bode plots which represent $\log|Z|$ and phase angle (θ) versus $\log(f)$. Bode plot was considered best fit to study the AC impedance data when wide range of frequency is covered [159]. Figure 4.9. Shows the equivalent circuit that was used to fit the obtained experimental data to explain the coating protection behavior. It consists of the electrolyte solution resistanceR_s, non-ideal double layer capacitances $CPE1\ and\ CPE2$ for the coating/solution and metal/solution interface interfaces respectively. R_{po} is the coatings pore resistanc, and the charge transfer resistance, R_{ct}, corresponds to the corrosion resistance at the metal/coating interface.

The high value of the frequency intercept $|Z_{100}kHz|$ corresponds to the solution resistance (R_s), while the lowest frequency intercept $|Z_{0.01}kHz|$ corresponds to the summation of the solution and charge transfer resistances($R_s + R_{ct}$) [160][161][162]. Since the prepared coatings were very porous, the double layer capacity C_{dl} can be determined form the given equation at maximum frequency [163]:

$$C_{dl} = {}^{1}/_{R_{ct}\omega_{max}} \qquad (4.4)$$

Where, $\omega_{max} = 2\pi f_{max}$ or by extrapolation and calculating slope of the straight line which usually in the range of -1 to ω= 1 rad.s^{-1}. In the diffusion control reaction as shown Nyquist plot by PSNI-2 and PSNI-3, Warburg impedance is calculated using the following equation [159]:

$$W = K(j\omega)^{\alpha} \qquad (4.5$$

If the value of $\alpha = -0.5$, W behaves as ideal diffusion impedance and $K = {}^{\sigma}/_{\sqrt{2}}$ where σ is the Warburg coefficient.

Gamry Echem analysis software was exploited to calculate impedance spectra parameters and analyze the obtained data. Nyquist plots of PS, PSNI-1, PSNI-2 and PSNI-3 shown in Figure 4.10 and 4.11. In these plots, the dots represent the measured points, while the solid lines represent the fitted data. The calculated electrochemical parameters extracted by the fitting EIS are summarized in Table 4.5

Bode plots shown in Figure 4.11 displays log |Z| versus log f and θ versuslog f, where |Z| the absolute value of the impedance, θ the phase angle, and f is the frequency (Hz). Bode magnitude plots are indicated there are two time constants. As clearly demonstrated that the anticorrosion performance of polystyrene has been enhanced by the addition of NiO nano-particles. It is found that the electrospun of 3:1 ratio of PS to NiO (PSNI-2) was considered as the optimal corrosion resistance coating with R= 750 $(k\Omega.cm^2)$. this result reflects the electrospinning technology is very efficient approach

to prepare good PS/NiO superhydrophobic coating for corrosion protection.

Table 4.5 briefly summarizes the EIS results of the electrospun PS and PS/NiO nanocomposite superhydrophobic coatings. The R_{ct} value increase with increasing the concentration of NiO nanoparticle as noticed in PSNI-1 and PSNI-2 which have R_{ct} equal 223.5 ($k\Omega.cm^2$) and $750(k\Omega.cm^2)$ respectively, while R_{ct} value is decreased in case of PSNI-3 to 82 ($k\Omega.cm^2$). This reduction in charge transfer resistance can be explained by the increase in the hydrophilic metal oxide (NiO) nanoparticles loading which leads to the formation of hydrogen bonds with water molecules and decrease the corrosion resistance of the coating [141]. However, the C_{dl} decreases with increasing the hydrophobicity of the coating which indicated the low permittivity of the prepared superhydrophobic coating. Constant phase element (CPE) is useful parameter to understand the electrochemical behavior of the material which is further depend to the value of surface heterogeneous (n). CPE is directly correlated to the construction of double layer at the metal solution interface [164] [163]. Also, surface heterogeneous (n) has value between 0 and 1, the n values of the prepared coatings are 0.0087, 0.0072, 0.0062 and 0.00765 for PS, PSNI-1, PSNI-2, and PSNI-3 respectively. These results verify that the electrospun PS/NiO with NiO concentration equal 0.026 M (PSNI-2) has the highest corrosion resistance of $(R_{ct} + R_p) = 850$ ($k\Omega.cm^2$) and lowest double layer capacitance C_{dl} equal 5.8×10^{-7} ($\mu F.cm^{-2}$) compared to other PS/NiO coatings. As well as, the Warburg diffusion (W) is reduced from 4.5×10^{-5} to $74.5\times 10^{-6}\Omega S^{-1/2}$. Consequently, PSNI-2 has the highest impedance parameters so perfect anticorrosion properties [165]. These values confirmed that the addition of NiO nanoparticles to PS achieves the superhydrophobic phenomenon of the material with large impedance and high corrosion resistance [166]. Also, this result agreed with AFM and WCA outcomes, which detect the great surface roughhouses and high water WCA

for PS/NiO nanocomposite SHC.

Table 4.5. Electrochemical parameters from Nyquist and Bode plots for aluminum substrates coating with pure PS and PS/NiO nanocomposite SHCs in 3.5 wt% NaCl solution.

Sample	WCA (°)	R_P $(k\Omega.cm^2)$	R_{ct} $(k\Omega.cm^2)$	Y_{01} $(\Omega^{-1}.cm^{-2}.sn) \times 10^{-6}$	n_1 x 10^{-3}	C_{dl1} $(\mu F.cm^{-2})$	Y_{02} $(\Omega^{-1}.cm^{-2}.sn) \times 10^{-6}$	n_2 x 10^{-3}	C_{dl2} $(\mu F.cm^{-2})$	W $\Omega.S^{-1/}$.
PS	148° ± 2°	5.120	49.00	9.664	870	8.6×10^{-6}	1.163	852	6.6×10^{-7}	-
PSNI-1	151° ± 2°	32	223.5	2.237	720	1.6×10^{-6}	0.00954	652	3.5×10^{-10}	-
PSNI-2	155° ± 2°	100	750	0.819	621	5.8×10^{-7}	0.00224	524	5.4×10^{-12}	74.5×10^{-6}
PSNI-3	150° ± 2°	25	82	3.905	765	2.7×10^{-6}	0.0124	681	4.7×10^{-10}	4.5×10^{-5}

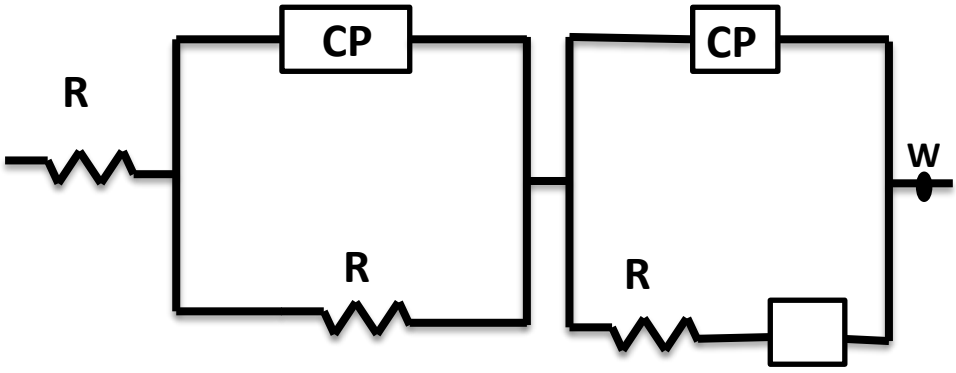

Figure 4.9. Equivalent electrical circuit used to fit the EIS spectra of Polystyrene and PS/NiO SHC in 3.5 wt % NaCl.

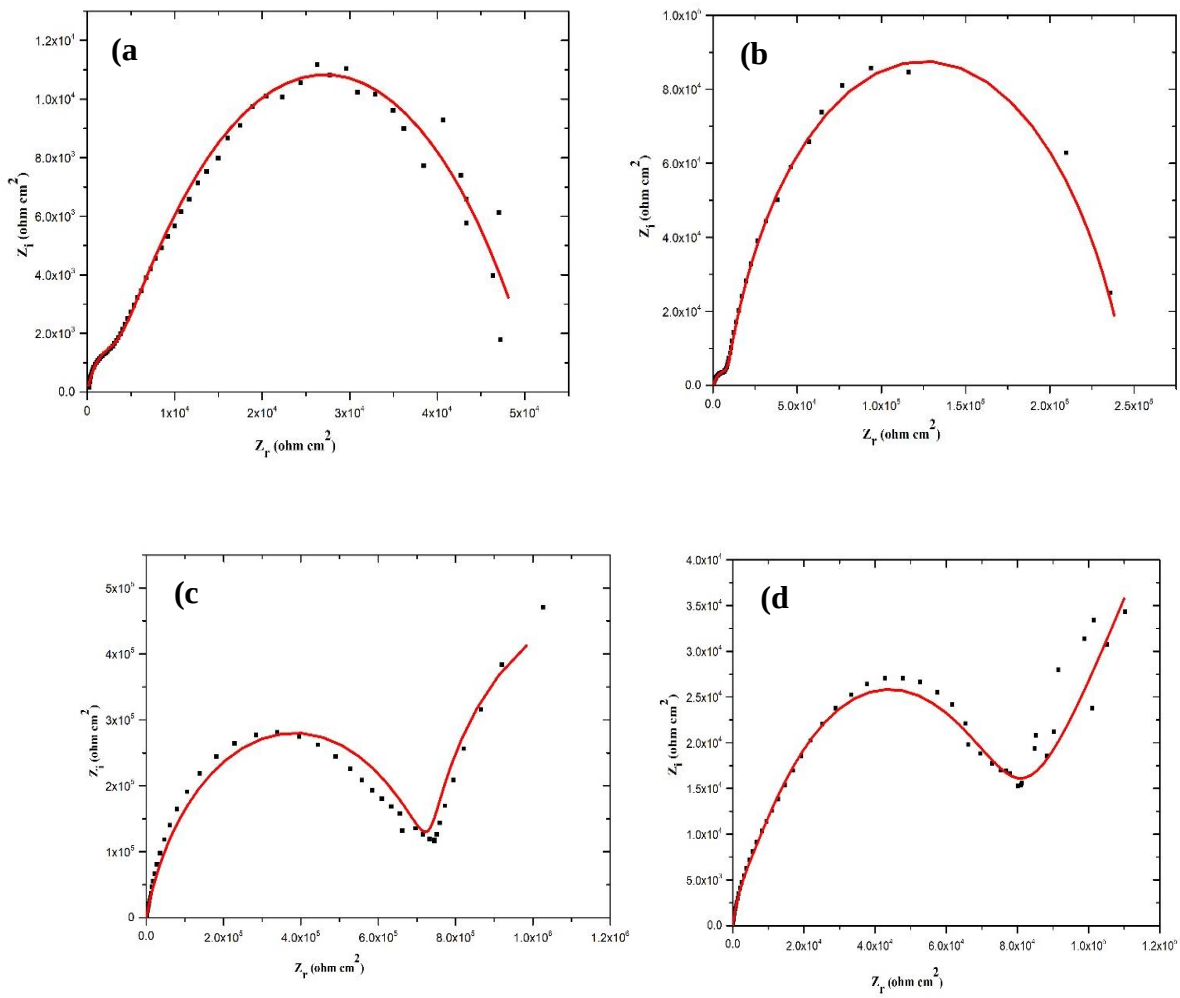

Figure 4.10. Nyquist Plots of EIS measurements of (a) PS, (b) PSNI-1, (c) PSNI-2 and (d) PSNI-3 in 3.5 wt% NaCl.

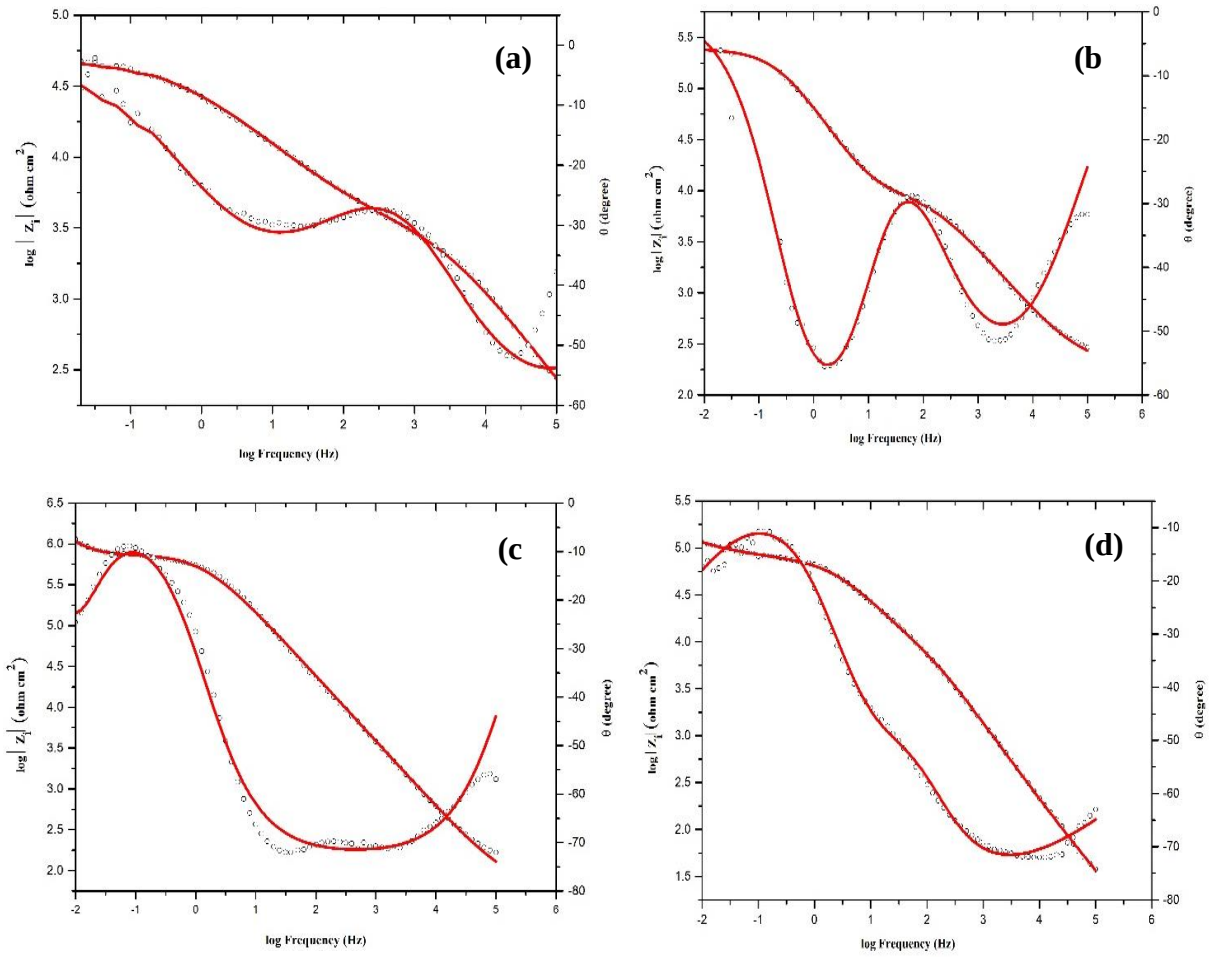

Figure 4.11. Bode plots of EIS measurements of (a) PS, (b) PSNI-1 (c) PSNI-2 and (d) PSNI-3 in 3.5 wt% NaCl.

CHAPTER 5: CONCLUSION

Polystyrene/nickel oxide (PS/NiO) nanocomposite superhydrophobic coatings were successfully fabricated via a one-step electrospinning technique. The electrospinning operational parameters that used to get the optimum result are 1.5 $mL.h^{-1}$ of flow rate, 18 kV of applied voltage and a distance of 15 cm with solution concentration of PS:NiO ratio of 1:10. The addition of NiO nanoparticles has a valuable effect on the wettability, surface roughness and thermal stability of neat polystyrene coating. The morphology of the prepared coating was characterized. It was proved to have a beaded fiber structure. The existence combination of microscale structure of the beads and nanoscale structure of the fibers improves the surface roughness of the coating as well as increasing WCA and decreasing CAH. It is confirmed that increasing NiO nanoparticle concentration decreases the diameters of the fibers. The highest water contact angle is obtained for PSNI-2 nanocomposite coating which was $155° \pm 2°$ and lowest contact hysteresis of 5°. Also, PSNI-2 showed the highest surface roughness with $R_{rms} = 27\ nm$.

From the above study, we concluded that a certain amount of NiO could reveal high corrosion resistance performance of PS coating on aluminum substrates. The synthesized PS/NiO nanocomposite superhydrophobic coating verified a significant increase in the corrosion protection of Al in 3.5 %wt NaCl solution. The corrosion behavior of the coatings was measured using impedance spectroscopy (EIS.) The superhydrophobic PS/NiO nanocomposite coating displayed a significant increase in corrosion resistance about 15 times higher than the corresponding corrosion resistance of pure PS under the same conditions. The highest corrosion resistance is measured for PSNI-2 which has Rct +R_p= 850 $(k\Omega.cm^2)$. However, increasing the concentration of NiO more than that amount can reduce the performance of corrosion protection of the

prepared coating. It is evidenced that the anti-corrosion properties of the nanocomposite coatings are referred to the high degree of superhydrophobicity of the coating instead of just acting as a barrier layer. On the other hand, the durability and the adhesion of the fabricated coating are the major issues associated with the superhydrophobic coatings. The improvement of the mechanical durability and transparency is the top priority of the development of the superhydrophobic surfaces.

In future work, dielectric properties of the nanocomposite coatings should be studied in order to recognize the conductivity of the material prepared that may be one of the factors which may affect the corrosion resistance efficiency as the nanoparticle concentration increased.

.

REFERENCES

[1] A. Bahgat Radwan, R. A. Shakoor, and A. Popelka, “Improvement in properties of Ni-B coatings by the addition of mixed oxide nanoparticles,” *Int. J. Electrochem. Sci.*, vol. 10, no. 9, pp. 7548–7562, 2015.

[2] R. Shakoor *et al.*, “Novel Electrodeposited Ni-B/Y2O3 Composite Coatings with Improved Properties,” *Coatings*, vol. 7, no. 10, p. 161, 2017.

[3] J. K. Wessel, *Handbook of Advanced Materials*. 2004.

[4] A. M. Abdel-Gaber, B. A. Abd-El-Nabey, I. M. Sidahmed, A. M. El-Zayady, and M. Saadawy, “Kinetics and thermodynamics of aluminium dissolution in 1.0 M sulphuric acid containing chloride ions,” *Mater. Chem. Phys.*, vol. 98, no. 2–3, pp. 291–297, 2006.

[5] B. Yin *et al.*, “Novel strategy in increasing stability and corrosion resistance for super-hydrophobic coating on aluminum alloy surfaces,” *Appl. Surf. Sci.*, vol. 258, no. 1, pp. 580–585, 2011.

[6] W. A. Badawy, F. M. Al-Kharafi, and A. S. El-Azab, “Electrochemical behaviour and corrosion inhibition of Al, Al-6061 and Al-Cu in neutral aqueous solutions,” *Corros. Sci.*, vol. 41, no. 4, pp. 709–727, 1999.

[7] W. Yang, Q. Li, Q. Xiao, and J. Liang, “Improvement of corrosion protective performance of organic coating on low carbon steel by PEO pretreatment,” *Prog. Org. Coatings*, vol. 89, pp. 260–266, 2015.

[8] D. A. Jones and M. M. Canada, “PrincipIes and Prevention of,” *Princ. Prev. Corros.*, 1992.

[9] L. Fedrizzi, F. J. Rodriguez, S. Rossi, F. Deflorian, and R. Di Maggio, “The use of electrochemical techniques to study the corrosion behaviour of organic coatings on steel pretreated with sol-gel zirconia films,” *Electrochim. Acta*, vol.

46, no. 24–25, pp. 3715–3724, 2001.

[10] A. B. Radwan, A. M. Abdullah, and M. K. Hassan, “Electrochemistry Communications The missing piece of the puzzle regarding the relation between the degree of superhydrophobicity and the corrosion resistance of superhydrophobic coatings,” *Electrochem. commun.*, vol. 91, no. May, pp. 41–44, 2018.

[11] Z. Zhou and X.-F. Wu, “Electrospinning superhydrophobic–superoleophilic fibrous PVDF membranes for high-efficiency water–oil separation,” *Mater. Lett.*, vol. 160, pp. 423–427, 2015.

[12] D. O. De and S. Wirtschaft, “Multiscale Dissipative Mechanisms and Hierarchical Surfaces Zu Inhaltsverzeichnis schnell und portofrei erhältlich bei,” 2008.

[13] B. P. Singh, B. K. Jena, S. Bhattacharjee, and L. Besra, “Surface & Coatings Technology Development of oxidation and corrosion resistance hydrophobic graphene oxide-polymer composite coating on copper,” *Surf. Coat. Technol.*, vol. 232, pp. 475–481, 2013.

[14] R. Kurbanova *et al.*, “Effects of the functional groups of polystyrene on its adhesion improvement and corrosion resistance,” vol. 4243, no. June, 2016.

[15] A. Kurganov, V. A. Davankov, B. Eray, K. K. Unger, and U. Trodinger, “Effect of polystyrene coating on pore , structural and chromatographic properties of silica packings,” vol. 506, 1990.

[16] K. Acatay, E. Simsek, C. Ow-yang, and Y. Z. Menceloglu, “Zuschriften,” pp. 5322–5325, 2004.

[17] W. Hou and Q. Wang, “Wetting behavior of a SiO 2 – polystyrene nanocomposite surface,” vol. 316, pp. 206–209, 2007.

[18] W. Hou and Q. Wang, “UV-Driven Reversible Switching of a Polystyrene / Titania Nanocomposite Coating between Superhydrophobicity and Superhydrophilicity,” vol. 25, no. c, pp. 6875–6879, 2009.

[19] X. Xu *et al.*, “Fabrication of Bionic Superhydrophobic Manganese Oxide / Polystyrene Nanocomposite Coating,” *J. Bionic Eng.*, vol. 9, no. 1, pp. 11–17, 2012.

[20] A. B. Radwan, A. M. Abdullah, and M. A. Al-maadeed, “New Electrospun Polystyrene/Al_2O_3 Nanocomposite Superhydrophobic Coatings; Synthesis, Characterization, and Application.”

[21] Y. Wang, B. Li, T. Liu, C. Xu, and Z. Ge, “Colloids and Surfaces A : Physicochemical and Engineering Aspects Controllable fabrication of superhydrophobic TiO_2 coating with improved transparency and thermostability,” *Colloids Surfaces A Physicochem. Eng. Asp.*, vol. 441, pp. 298–305, 2014.

[22] G. Liu, L. Qiao, and A. Guo, “Diblock Copolymer Nanofibers,” pp. 5508–5510, 1996.

[23] A. Bahgat Radwan, A. M. Abdullah, and N. A. Alnuaimi, “Recent advances in corrosion resistant superhydrophobic coatings,” *Corros. Rev.*, 2017.

[24] E. Process, J. Doshi, and D. H. Reneker, “Journal of,” vol. 35, pp. 151–160, 1995.

[25] K. H. Lee, H. Y. Kim, H. J. Bang, Y. H. Jung, and S. G. Lee, “The change of bead morphology formed on electrospun polystyrene fibers,” vol. 44, pp. 4029–4034, 2003.

[26] Z. Huang, Y. Zhang, M. Kotaki, and S. Ramakrishna, “A review on polymer nanofibers by electrospinning and their applications in nanocomposites,” vol. 63,

pp. 2223–2253, 2003.

[27] J. M. Deitzel, J. Kleinmeyer, D. Harris, and N. C. B. Tan, “The effect of processing variables on the morphology of electrospun nanofibers and textiles,” vol. 42, pp. 261–272, 2001.

[28] S. Sukigara, M. Gandhi, J. Ayutsede, M. Micklus, and F. Ko, “Regeneration of Bombyx mori silk by electrospinning — part 1 : processing parameters and geometric properties,” vol. 44, pp. 5721–5727, 2003.

[29] M. M. Demir, I. Yilgor, E. Yilgor, and B. Erman, “Electrospinning of polyurethane ® bers,” vol. 43, pp. 3303–3309, 2002.

[30] H. Fong, I. Chun, and D. H. Reneker, “Beaded nanofibers formed during electrospinning,” vol. 40, pp. 4585–4592, 1999.

[31] D. L. Hu and J. W. M. Bush, “Meniscus-climbing insects,” vol. 437, no. September, pp. 733–736, 2005.

[32] B. W. Min, B. Jiang, and P. Jiang, “Bioinspired Self-Cleaning Antireflection Coatings **,” pp. 3914–3918, 2008.

[33] C. Article, “Nanoscale Superhydrophobic gecko feet with high adhesive forces towards water and,” vol. 4, no. 3, 2012.

[34] M. Tang, X. Huang, J. Yu, X. Li, and Q. Zhang, “Simple Fabrication of Large-Area Corrosion Resistant Superhydrophobic Surface with High Mechanical Strength Property on TiAl- based Composite,” *J. Mater. Process. Tech.*, 2016.

[35] H. Wang, X. Zhang, Z. Liu, Y. Zhu, S. Wu, and Y. Zhu, “RSC Advances,” *RSC Adv.*, vol. 6, pp. 10930–10937, 2016.

[36] A. Bo, Z. Haitao, F. Feng, L. Yabin, and W. Liping, “Accepted Manuscript,” 2016.

[37] V. A. Online *et al.*, “RSC Advances,” 2016.

[38] P. Taylor and S. H. Kim, “Journal of Adhesion Science and Fabrication of Superhydrophobic Surfaces,” no. September, pp. 37–41, 2012.

[39] M. Strobel and C. S. Lyons, “An Essay on Contact Angle Measurements,” pp. 8–13, 2011.

[40] D. Gennes, “statics and dynamics,” vol. 57, no. 3, 1985.

[41] M. Per, “RESISTANCE OF SOLID SURFACES,” pp. 988–994.

[42] B. Leng, Z. Shao, G. De With, and W. Ming, “Superoleophobic Cotton Textiles,” no. 29, pp. 2456–2460, 2009.

[43] M. Nosonovsky and B. Bhushan, “Current Opinion in Colloid & Interface Science Superhydrophobic surfaces and emerging applications : Non-adhesion , energy , green engineering,” *Curr. Opin. Colloid Interface Sci.,* vol. 14, no. 4, pp. 270–280, 2009.

[44] R. G. Karunakaran, C. Lu, Z. Zhang, and S. Yang, “Highly Transparent Superhydrophobic Surfaces from the Coassembly of Nanoparticles (e 100 nm),” pp. 4594–4602, 2011.

[45] P. Zhang and F. Y. Lv, “A review of the recent advances in superhydrophobic surfaces and the emerging energy-related applications,” 2015.

[46] X. Zhang, F. Shi, J. Niu, Y. Jiang, and Z. Wang, “Superhydrophobic surfaces : from structural control to functional application,” pp. 621–633, 2008.

[47] L. Yao and J. He, “Progress in Materials Science Recent progress in antireflection and self-cleaning technology – From surface engineering to functional surfaces,” *Prog. Mater. Sci.,* vol. 61, pp. 94–143, 2014.

[48] G. Barati, M. Aliofkhazraei, S. Khorsand, S. Sokhanvar, and A. Kaboli, “Science and Engineering of Superhydrophobic Surfaces : Review of Corrosion Resistance , Chemical and Mechanical Stability,” *Arab. J. Chem.,* 2018.

[49] D. Qu, “Non-sticking drops,” vol. 2495, 2005.

[50] M. Nosonovsky and B. Bhushan, “Roughness-induced superhydrophobicity : a way to design non-adhesive surfaces,” vol. 225009, 2008.

[51] B. Krasovitski and A. Marmur, “Drops Down the Hill : Theoretical Study of Limiting Contact Angles and the Hysteresis Range on a Tilted Plate,” no. 22, pp. 3881–3885, 2005.

[52] W. Chen, A. Y. Fadeev, M. C. Hsieh, O. Didem, J. Youngblood, and T. J. Mccarthy, “Ultrahydrophobic and Ultralyophobic Surfaces : Some Comments and Examples,” no. 13, pp. 3395–3399, 1999.

[53] B. Bhushan, Y. C. Jung, and K. Koch, “Micro- , nano- and hierarchical structures for superhydrophobicity , self-cleaning and low adhesion,” 2009.

[54] W. Xu, J. Song, J. Sun, Y. Lu, and Z. Yu, “Rapid Fabrication of Large-Area , Corrosion-Resistant Superhydrophobic Mg Alloy Surfaces,” pp. 4404–4414, 2011.

[55] R. Taurino, E. Fabbri, M. Messori, F. Pilati, D. Pospiech, and A. Synytska, “Journal of Colloid and Interface Science Facile preparation of superhydrophobic coatings by sol – gel processes,” vol. 325, pp. 149–156, 2008.

[56] W. Y. Gan, W. Lam, K. Chiang, R. Amal, and M. Paul, “Novel TiO 2 thin film with non-UV activated superwetting and antifogging behaviours {,” pp. 952–954, 2007.

[57] M. Nicolas and S. Ge, “Stable Superhydrophobic and Lipophobic Conjugated Polymers Films,” no. 11, pp. 3081–3088, 2006.

[58] S. Amigoni, E. T. De Givenchy, and M. Dufay, “Covalent Layer-by-Layer Assembled Superhydrophobic Organic - Inorganic Hybrid Films,” vol. 25, no. 14, pp. 11073–11077, 2009.

[59] L. Huang, S. P. Lau, H. Y. Yang, E. S. P. Leong, and S. F. Yu, “Stable Superhydrophobic Surface via Carbon Nanotubes Coated with a ZnO Thin Film,” pp. 7746–7748, 2010.

[60] M. Peng, H. Li, L. Wu, Q. Zheng, Y. Chen, and W. Gu, “Porous Poly (Vinylidene Fluoride) Membrane with Highly Hydrophobic Surface,” 2005.

[61] L. P. Milaor, F. Dela Cruz, and R. F. Pobre, “Synthesis and Characterization of a Silica-based Hydrophobic Coating using Sol-Gel Method Applied on Various Substrates Presented at the DLSU Research Congress 2017,” 2017.

[62] X. Zhang, R. Chen, Y. Liu, and J. Hu, “inhibitor containers of superhydrophobic surfaces for the active corrosion protection of metals †,” pp. 649–656, 2016.

[63] N. Wang and D. Xiong, “Superhydrophobic membranes on metal substrate and their corrosion protection in different corrosive media,” *Appl. Surf. Sci.*, vol. 305, pp. 603–608, 2014.

[64] J. Liang, Y. Hu, Y. Wu, and H. Chen, “Surface & Coatings Technology Facile formation of superhydrophobic silica-based surface on aluminum substrate with tetraethylorthosilicate and vinyltriethoxysilane as co-precursor and its corrosion resistant performance in corrosive NaCl aqueous solution,” *Surf. Coat. Technol.*, vol. 240, pp. 145–153, 2014.

[65] J. Lee and W. Hwang, “Exploiting the silicon content of aluminum alloys to create a superhydrophobic surface using the sol – gel process,” *Mater. Lett.*, vol. 168, pp. 83–85, 2016.

[66] T. Rezayi and M. H. Entezari, “Journal of Colloid and Interface Science Toward a durable superhydrophobic aluminum surface by etching and ZnO nanoparticle deposition,” *J. Colloid Interface Sci.*, vol. 463, pp. 37–45, 2016.

[67] Y. Huang, D. K. Sarkar, and X. G. Chen, “Ac ce pt e cr t,” *Appl. Surf. Sci.*, 2015.

[68] M. Ma and R. M. Hill, “Superhydrophobic surfaces,” vol. 11, pp. 193–202, 2006.

[69] B. K. Teshima, H. Sugimura, Y. Inoue, O. Takai, and A. Takano, “(a) 500,” pp. 295–297, 2004.

[70] B. Qian and Z. Shen, “Fabrication of Superhydrophobic Surfaces by Dislocation-Selective Chemical Etching on Aluminum , Copper , and Zinc Substrates,” no. 19, pp. 9007–9009, 2005.

[71] C. Resistance, “One-Step Preparation of Super-Hydrophobic.”

[72] I. Interactions, T. Shi, X. Li, Q. Zhang, and B. Li, “One-Step Potentiostatic Deposition of Micro-Particles on Al Alloy as Superhydrophobic Surface for Enhanced Corrosion Resistance by Reducing.”

[73] Y. Liu, H. Cao, Y. Chen, and D. Wang, “RSC Advances with corrosion resistance on copper substrate,” pp. 2379–2386, 2016.

[74] B. Zhang and B. Hou, “RSC Advances One-step electrodeposition fabrication of a superhydrophobic surface on an aluminum substrate with enhanced self-cleaning and,” pp. 100000–100010, 2015.

[75] B. Zhang, X. Zhao, and B. Hou, “RSC Advances Fabrication of durable anticorrosion superhydrophobic surfaces on aluminum substrates via a facile one-step electrodeposition,” pp. 35455–35465, 2016.

[76] K. Saeed and S. Park, “Preparation and characterization of multiwalled carbon nanotubes / polyacrylonitrile nanofibers,” pp. 535–540, 2010.

[77] W. Ponhan and S. Maensiri, “Fabrication and magnetic properties of electrospun copper ferrite (CuFe 2 O 4) nanofibers,” *Solid State Sci.*, vol. 11, no. 2, pp. 479–484, 2009.

[78] K. Acatay, E. Simsek, C. Ow-yang, and Y. Z. Menceloglu, “Tunable, Superhydrophobically Stable Polymeric Surfaces by Electrospinning**,” pp.

5210–5213, 2004.

[79] A. B. Radwan, A. M. A. Mohamed, A. M. Abdullah, and M. A. Al-Maadeed, “Corrosion protection of electrospun PVDF-ZnO superhydrophobic coating,” *Surf. Coatings Technol.*, vol. 289, pp. 136–143, 2016.

[80] N. Okutan, P. Terzi, and F. Altay, “Food Hydrocolloids Affecting parameters on electrospinning process and characterization of electrospun gelatin nano fi bers,” vol. 39, pp. 19–26, 2014.

[81] N. Bhardwaj and S. C. Kundu, “Electrospinning : A fascinating fi ber fabrication technique,” vol. 28, pp. 325–347, 2010.

[82] “Science and Technology of Polymer Nanofibers.,” no. September 2006, p. 808193, 2008.

[83] J. Ratanavaraporn, R. Rangkupan, and H. Jeeratawatchai, “International Journal of Biological Macromolecules Influences of physical and chemical crosslinking techniques on electrospun type A and B gelatin fiber mats,” *Int. J. Biol. Macromol.*, vol. 47, no. 4, pp. 431–438, 2010.

[84] X. Chen *et al.*, “Electrospun Magnetic Fibrillar Polystyrene Nanocomposites Reinforced with Nickel Nanoparticles,” pp. 1775–1783, 2010.

[85] J. Liang, Y. Hu, Y. Wu, and H. Chen, “Fabrication and Corrosion Resistance of Superhydrophobic Hydroxide Zinc Carbonate Film on Aluminum Substrates,” vol. 2013, 2013.

[86] Y. Hu, S. Huang, S. Liu, and W. Pan, “Applied Surface Science A corrosion-resistance superhydrophobic TiO 2 film,” vol. 258, pp. 7460–7464, 2012.

[87] “No Title,” no. November, pp. 1–10, 1999.

[88] S. Megelski, J. S. Stephens, D. B. Chase, and J. F. Rabolt, “Micro- and Nanostructured Surface Morphology on Electrospun Polymer Fibers,” pp. 8456–

8466, 2002.

[89] P. Taylor, “APPLICATION OF ELECTROSPUN POLYSTYRENE NANOFIBERS AS SOLID PHASE EXTRACTION SORBENT FOR THE PRECONCENTRATION OF DIAZINON AND,” no. September 2014, pp. 37–41.

[90] M. G. Hajra, K. Mehta, and G. G. Chase, “Effects of humidity , temperature , and nanofibers on drop coalescence in glass fiber media,” vol. 30, pp. 79–88, 2003.

[91] H. Lee *et al.*, “Electrospun tri-layered zein / PVP-GO / zein nano fi ber mats for providing biphasic drug release pro fi les,” *Int. J. Pharm.*, vol. 531, no. 1, pp. 101–107, 2017.

[92] Z. Tang *et al.*, “UV-cured poly (vinyl alcohol) ultrafiltration nanofibrous membrane based on electrospun nanofiber scaffolds,” vol. 328, pp. 1–5, 2009.

[93] L. Pan, D. Lolla, G. Chase, and G. George, “Functionalized Polyvinylidene Polyvinylidene Fluoride Fluoride Electrospun Electrospun Nanofibers and Applications Applications Dinesh,” 2018.

[94] H. Lee *et al.*, “polyvinyl alcohol composite separator membranes : A membrane-driven step closer toward rechargeable zinc – air batteries,” *J. Memb. Sci.*, vol. 499, pp. 526–537, 2016.

[95] E. Llorens, H. Ibañez, L. J. Valle, and J. Puiggalí, “Biocompatibility and drug release behavior of scaffolds prepared by coaxial electrospinning of poly (butylene succinate) and polyethylene glycol,” *Mater. Sci. Eng. C*, vol. 49, pp. 472–484, 2015.

[96] C. Xu, F. Xu, B. Wang, and T. Lu, “Electrospinning of Poly (ethylene-co-vinyl alcohol) Nanofibres Encapsulated with Ag Nanoparticles for Skin Wound

Healing," vol. 2011, 2011.

[97] M. Ignatova, N. Markova, N. Manolova, and I. Rashkov, "Journal of Biomaterials Science , Antibacterial and antimycotic activity of a cross-linked electrospun poly (vinyl pyrrolidone)– iodine complex and a poly (ethylene oxide)/ poly (vinyl pyrrolidone)– iodine complex," no. September 2014, pp. 37–41, 2012.

[98] X. Qin and S. Wang, "Electrospun Nanofibers from Crosslinked Poly (vinyl alcohol) and Its Filtration Efficiency," vol. 109, no. November 2007, pp. 951–956, 2008.

[99] B. Maddah, M. Soltaninezhad, and K. Adib, "Activated carbon nanofiber produced from electrospun PAN nanofiber as a solid phase extraction sorbent for the preconcentration of organophosphorus pesticides," *Sep. Sci. Technol.*, vol. 52, no. 4, pp. 700–711, 2017.

[100] S. Kaur, R. Barhate, S. Sundarrajan, T. Matsuura, and S. Ramakrishna, "Hot pressing of electrospun membrane composite and its in fl uence on separation performance on thin fi lm composite nano fi ltration membrane," vol. 279, pp. 201–209, 2011.

[101] I. W. Baek, J. Y. Jaung, and S. H. Kim, "Molecular Crystals and Liquid Crystals Electrospinning of Polycarbonate / Tetrapyrazinoindoloporphyrazine Composite Fibers," no. October 2014, pp. 37–41.

[102] H. Tong and M. Wang, "Electrospinning of Poly (hydroxybutyrate- co - hydroxyvalerate) Fibrous Tissue Engineering Scaffolds in Two Different Electric Fields," no. 1, 2011.

[103] Æ. G. A. Abraham, "Electrospinning of novel biodegradable poly (ester urethane) s and poly (ester urethane urea) s for soft tissue-engineering

applications," pp. 2129–2137, 2009.

[104] C. Yao, X. Li, K. G. Neoh, Z. Shi, and E. T. Kang, "Surface modification and antibacterial activity of electrospun polyurethane fibrous membranes with quaternary ammonium moieties," vol. 320, pp. 259–267, 2008.

[105] F. Basiri, S. Abdolkarim, H. Ravandi, M. Feiz, and A. Moheb, "Recycling of Direct Dyes Wastewater by Nylon-6 Nanofibrous Membrane," pp. 633–639, 2011.

[106] A. Manuscript, "Materials Chemistry A," 2016.

[107] T. Suryaprabha and M. Gopalakrishnan, "Fabrication of copper-based superhydrophobic self-cleaning antibacterial coating over cotton fabric," *Cellulose*, 2016.

[108] J. Gao, X. Huang, H. Xue, L. Tang, and R. K. Y. Li, "Facile preparation of hybrid microspheres for super-hydrophobic coating and oil-water separation," *Chem. Eng. J.*, 2017.

[109] X. Y. Liu, Z. P. Wang, B. G. Fu, L. Long, X. L. Zhang, and H. X. Cui, "Effects of Mg content on the mechanical properties and corrosion resistance of Al e Cu e Mg e Ag alloy Hardness / HV Time / h," *J. Alloys Compd.*, vol. 685, pp. 209–215, 2016.

[110] J. Li *et al.*, "Fabrication of stable Ni – Al 4 Ni 3 – Al 2 O 3 superhydrophobic surface on aluminum substrate for self-cleaning , anti-corrosive and catalytic performance," 2017.

[111] T. Shi, J. Kong, X. Wang, and X. Li, "Applied Surface Science Preparation of multifunctional Al-Mg alloy surface with hierarchical micro / nanostructures by selective chemical etching processes," *Appl. Surf. Sci.*, vol. 389, pp. 335–343, 2016.

[112] N. Wang, D. Xiong, Y. Deng, Y. Shi, and K. Wang, “Mechanically Robust Superhydrophobic Steel Surface with Anti- Icing, UV-Durability, and Corrosion Resistance Properties,” 2015.

[113] T. Leung, W. K. Talley, and D. Jin, “The effectiveness of double hulls in reducing vessel-accident oil spillage,” *Mar. Pollut. Bull.*, vol. 62, no. 11, pp. 2427–2432, 2011.

[114] H. Li and M. C. Boufadel, “Long-term persistence of oil from the Exxon Valdez spill in two-layer beaches,” *Nat. Geosci.*, vol. 3, no. 2, pp. 96–99, 2010.

[115] G. Wang *et al.*, “and under-water superoleophobicity for highly,” pp. 3093–3099, 2015.

[116] O. Arslan, Z. Aytac, and T. Uyar, “Superhydrophobic , Hybrid , Electrospun Cellulose Acetate Nano fi brous Mats for Oil / Water Separation by Tailored Surface Modi fi cation,” 2016.

[117] Y. Fu, B. Jin, Q. Zhang, X. Zhan, and F. Chen, “pH-Induced Switchable Superwettability of E ffi cient Antibacterial Fabrics for Durable Selective Oil / Water Separation,” 2017.

[118] X. Su *et al.*, “Dual-Functional Superhydrophobic Textiles with Asymmetric Roll-Down/Pinned States for Water Droplet Transportation and Oil–Water Separation,” 2018.

[119] A. Kumar and B. Gogoi, “Tribology International Development of durable self-cleaning superhydrophobic coatings for aluminium surfaces via chemical etching method,” *Tribol. Int.*, vol. 122, no. January, pp. 114–118, 2018.

[120] S. S. Latthe, R. S. Sutar, V. S. Kodag, A. K. Bhosale, and A. M. Kumar, “Progress in Organic Coatings Self – cleaning superhydrophobic coatings : Potential industrial applications,” *Prog. Org. Coatings*, vol. 128, no. August

2018, pp. 52–58, 2019.

[121] A. Manuscript, “Materials Chemistry A,” 2015.

[122] R. Materials, “results demonstrate that this limitation can be cir- cumvented by operating below the length scale determined by the electron mean free path.,” 2013.

[123] S. Zheng *et al.*, “NU SC College of Materials Science and Technology , Nanjing University of Aeronautics and,” *JMADE*, 2015.

[124] Z. Wang, J. Ou, Y. Wang, M. Xue, and F. Wang, “NU SC,” *Surf. Coat. Technol.*, 2015.

[125] B. J. Privett *et al.*, “Antibacterial Fluorinated Silica Colloid Superhydrophobic Surfaces,” pp. 9597–9601, 2011.

[126] C. Xue, J. Chen, W. Yin, S. Jia, and J. Ma, “Applied Surface Science Superhydrophobic conductive textiles with antibacterial property by coating fibers with silver nanoparticles,” *Appl. Surf. Sci.*, vol. 258, no. 7, pp. 2468–2472, 2012.

[127] H. Zhu *et al.*, “Graphical abstract A dual-layer copper mesh consists of a superhydrophobic Ag-coated mesh and a photocatalytic GO / AgBr-coated mesh was fabricated for water purification via separation of insoluble oil from water and successively photodegradation of,” *"Applied Catal. B, Environ.*, 2016.

[128] X. Lu *et al.*, “Surface & Coatings Technology Antifogging and antire fl ective silica fi lm and its application on solar modules,” vol. 206, pp. 1490–1494, 2011.

[129] P. Wang, D. Zhang, R. Qiu, and B. Hou, “Super-hydrophobic film prepared on zinc as corrosion barrier,” *Corros. Sci.*, vol. 53, no. 6, pp. 2080–2086, 2011.

[130] P. G. Pawar, R. Xing, R. C. Kambale, A. M. Kumar, S. Liu, and S. S. Latthe, “Progress in Organic Coatings Polystyrene assisted superhydrophobic silica

coatings with surface protection and self-cleaning approach," *Prog. Org. Coatings*, vol. 105, pp. 235–244, 2017.

[131] Y. Liu, H. Cao, S. Chen, and D. Wang, "Ag Nanoparticle-Loaded Hierarchical Superamphiphobic Surface on an Al Substrate with Enhanced Anticorrosion and Antibacterial Properties," 2015.

[132] J. Nine, M. A. Cole, L. Johnson, D. N. H. Tran, and D. Losic, "Robust Superhydrophobic Graphene-Based Composite Coatings with Self-Cleaning and Corrosion Barrier Properties," no. Cvd, 2015.

[133] M. Wang *et al.*, "ZnO Nanorod Array Modi fi ed PVDF Membrane with Superhydrophobic Surface for Vacuum Membrane Distillation Application," 2018.

[134] T. Ren *et al.*, "CuO Nanoparticles-Containing Highly Transparent and Superhydrophobic Coatings with Extremely Low Bacterial Adhesion and Excellent Bactericidal Property," *ACS Appl. Mater. Interfaces*, vol. 10, pp. 25717–25725, 2018.

[135] Y. Zhou *et al.*, "Robust Superhydrophobic Surface Based on Multiple Hybrid Coatings for Application in Corrosion Protection," *ACS Appl. Mater. Interfaces*, vol. 11, pp. 6512–6526, 2019.

[136] B. Wang *et al.*, "Methodology for Robust Superhydrophobic Fabrics and Sponges from In Situ Growth of Transition Metal / Metal Oxide Nanocrystals with Thiol Modi fi cation and Their Applications in Oil / Water Separation," 2013.

[137] M. Zhang, P. Wang, H. Sun, and Z. Wang, "Superhydrophobic Surface with Hierarchical Architecture and Bimetallic Composition for Enhanced Antibacterial Activity," 2014.

[138] N. Zhan *et al.*, “Journal of Colloid and Interface Science A novel multinozzle electrospinning process for preparing superhydrophobic PS films with controllable bead-on-string / microfiber morphology,” *J. Colloid Interface Sci.*, vol. 345, no. 2, pp. 491–495, 2010.

[139] T. Jarusuwannapoom and W. Hongrojjanawiwat, “EUROPEAN POLYMER Effect of solvents on electro-spinnability of polystyrene solutions and morphological appearance of resulting electrospun polystyrene fibers,” vol. 41, pp. 409–421, 2005.

[140] Z. Zhou, W. Ruan, H. Huang, C. Shen, B. Yuan, and C. Huang, “Fabrication and characterization of Fe / Ni nanoparticles supported by polystyrene resin for trichloroethylene degradation,” *Chem. Eng. J.*, 2015.

[141] E. Murat, C. E. Cansoy, and E. Ozkan, “Progress in Organic Coatings Investigation of wettability and optical properties of superhydrophobic polystyrene-SiO 2 composite surfaces,” *Prog. Org. Coatings*, vol. 99, pp. 378–385, 2016.

[142] B. D. Cassie, “Of porous surfaces,” no. 5, pp. 546–551, 1944.

[143] Y. Zhao, C. Xing, Z. Zhang, and L. Yu, “Superhydrophobic polyaniline / polystyrene micro / nanostructures as anticorrosion coatings,” *React. Funct. Polym.*, vol. 119, no. February, pp. 95–104, 2017.

[144] S. Chemistry, “Fakir droplets,” vol. 1, no. September, pp. 14–15, 2002.

[145] H. Assembly, “Contact Angle Measurements Using a Simplified Experimental Setup,” vol. 87, no. 12, pp. 1403–1407, 2010.

[146] A. Hooda, M. S. Goyat, R. Gupta, M. Prateek, and M. Agrawal, “Synthesis of nano-textured polystyrene / ZnO coatings with excellent transparency and superhydrophobicity,” *Mater. Chem. Phys.*, vol. 193, pp. 447–452, 2017.

[147] M. El-kemary and N. Nagy, “Materials Science in Semiconductor Processing Nickel oxide nanoparticles : Synthesis and spectral studies of interactions with glucose $,” *Mater. Sci. Semicond. Process.*, vol. 16, no. 6, pp. 1747–1752, 2013.

[148] F. Davar, Z. Fereshteh, and M. Salavati-niasari, “Nanoparticles Ni and NiO : Synthesis , characterization and magnetic properties,” vol. 476, pp. 797–801, 2009.

[149] A. Hooda, A. Kumar, and R. Gupta, “A facile approach to develop modified nano-silica embedded polystyrene based transparent superhydrophobic coating,” *Mater. Lett.*, 2018.

[150] E. Soleimani and M. Mohammadi, “Synthesis , characterization and properties of polystyrene / NiO nanocomposites,” *J. Mater. Sci. Mater. Electron.*, vol. 0, no. 0, p. 0, 2018.

[151] M. C. Æ. B. Hwang, “Transformation of b -Ni (OH) 2 to NiO nano-sheets via surface nanocrystalline zirconia coating : Shape and size retention,” pp. 28–33, 2007.

[152] Y. Chung, S. R. Yun, C. W. Lee, N. Jo, C. Yo, and K. Ryu, “Inorganic / Organic Nanocomposites of Polyaniline and Fe 3 O 4 with Hollow Cluster Structures using Polystyrene Template,” vol. 31, no. 7, pp. 3–6, 2010.

[153] X. Yan *et al.*, “Magnetic Polystyrene Nanocomposites Reinforced with Magnetite Nanoparticles,” pp. 485–494, 2014.

[154] E. Industrial, “Glass Transition Measurements on Polystyrene by Differential Scanning Calorimetry,” pp. 319–326.

[155] P. Pellets, “Differential Scanning Calorimetry of Polystyrene.”

[156] E. S. P. B. V, A. J. Pasztor, B. G. Landes, P. J. Karjala, T. Dow, and C. Company, “The early development of polystyrene is , in fact , the development of atactic

polystyrene . Figure 1 shows that atactic polystyrene is characterized by the phenyl rings having a random orientation relative to the polymer chain backbone . In the 1950s a method was developed for the synthesis of isotactic polystyrene , which is characterized by having all of the phenyl rings on the same side of the polymer backbone (Fig . 1). The production of isotactic polystyrene gave the first crystallizable form of polystyrene . The relatively high melting point (240 O C) gives isotactic polystyrene good solvent resistance and added strength at temperatures above Tg . Attempts to com- mercialize isotactic polystyrene met with limited success , due in large part to the relatively slow crystallization rate . In the last three years , several authors have described the preparation of syndiotactic polystyrene [l-4]. Syndiotactic polystyrene differs from the," vol. 77, pp. 187–195, 1991.

[157] R. Asaletha, M. G. Kumaran, and S. Thorna, "Thermal behaviour of natural rubber / polystyrene blends : thermogravimetric and differential scanning calorimetric analysis," vol. 61, pp. 431–439, 1998.

[158] L. A. Garcı, "Synthesis and characterization of NiO nanoparticles and their PMMA nanocomposites obtained by in situ bulk polymerization," pp. 4553–4556, 2009.

[159] F. Mansfeld, M. W. Kendig, and S. Tsai, "Evaluation of Corrosion Behavior of Coated Metals with AC Impedance Measurements *," pp. 478–485, 1982.

[160] N. N. Nanocomposites, "Synthesis, Characterization, and Application of Novel Ni-P-Carbon Nitride Nanocomposites," pp. 1–13, 2018.

[161] D. Yang *et al.*, "Original article Electrochemical and XPS studies of alkyl imidazoline on the corrosion inhibition of carbon steel in citric acid solution," 2016.

[162] S. Kadapparambil, K. Yadav, M. Ramachandran, and N. V. Selvam, “Original article Electrochemical investigation of the corrosion inhibition mechanism of Tectona grandis leaf extract for SS304 stainless steel in hydrochloric acid,” 2017.

[163] S. Dahiya, S. Lata, P. Kumar, and R. Kumar, “Original article A descriptive study for corrosion control of low-alloy steel by Aloe vera extract in acidic medium,” vol. 34, no. 4, pp. 241–248, 2016.

[164] R. Kumar, S. Chahal, S. Dahiya, N. Dahiya, S. Kumar, and S. Lata, “Original article Experimental and theoretical approach to exploit the corrosion inhibition activity of 3-formyl chromone derivatives on mild steel in 1 m H 2 SO 4,” 2017.

[165] Y. Zhao, Z. Zhang, and L. Yu, “Corrosion protection of carbon steel by electrospun film containing polyaniline microfibers,” *React. Funct. Polym.*, vol. 102, pp. 20–26, 2016.

[166] Y. Sun, D. Zhao, J. Song, C. Wang, Z. Zhang, and L. Huang, “Results in Physics Rapid fabrication of superhydrophobic high-silicon aluminum alloy surfaces with corrosion resistance,” *Results Phys.*, vol. 12, no. November 2018, pp. 1082–1088, 2019.